Geothermics 105 (2022) 102474

Contents lists available at ScienceDirect

Geothermics

journal homepage: www.elsevier.com/locate/geothermics

Magma fracking and production reservoirs beneath and adjacent to Mutnovsky volcano based on seismic data and hydrothermal activity

A.V. Kiryukhin [a,*], A.Y. Polyakov [a], P.O. Voronin [a], N.B. Zhuravlev [a], O.O. Usacheva [a], A.V. Solomatin [a], P.A. Kiryukhin [b]

[a] *Institute of Volcanology & Seismology FEB RAS, Piip 9, Petropavlovsk-Kamchatsky 683006, Russia*
[b] *EPAM, Zastavskaya 22-2, Saint Petersburg 196084 Russia*

ARTICLE INFO

Key words:
Magma
Injections
MEQ
Mutnovsky
Production
NCG
Hydromechanical
model

ABSTRACT

Mutnovsky geothermal area in Kamchatka, Russia where 62 MWe GeoPP installed - is a source of geothermal electricity supply, as well as a hazard volcanic area. We used local seismicity micro-earthquakes (MEQ's) data from 2009 to 2021 to define seismogenic faults beneath and adjacent to Mutnovsky volcano, which interpreted as magma injections in form of dykes and sills. Magma fracking beneath Mutnovsky volcano pointed on shear mode low angle dykes in northeast sector and opening mode geomechanical conditions at -3000 m, where sills in area of 62 km^2 are suggested to be formed. Low angle dykes injections were reproduced by hydromechanical simulation using CFRAC, modeling results matches with MEQ's statistics observed.

Mutnovsky GeoPP steam collection system shows sensitivity to non-condensable gasses (NCG) content (partial gas pressure) variations (2019—2020), that is used as indicator of magmatic gasses recharge via magma fracking volcano system to production geothermal reservoir. Partial gas pressure measured at GeoPP condenser unit. Magma injections associated with NCG (CO_2) release in production reservoirs seems to be synchronize with partial NCG pressure excursions at GeoPP condenser. Some signs of magma fracking events were also revealed using discreet observations (2016–2021) on a blowing wells on a foothills of Mutnovsky volcano. Magma fracking beneath Mutnovsky volcano is associate with small and medium hydrothermal explosions and landslide (2009–2021). Magma fracking distributions pointed on a new potentially production geothermal reservoir beneath northeast foothills of Mutnovsky volcano (depth range from -4000 to -2000 m, accessible area of 30 km^2).

1. Introduction

1.1. Statement of the problem

Volcanoes and crustal magmatic chambers are products of magmatic injections from primary magmatic sources located at depths of 150 to 200 km (Fedotov, 2006) in the area of the active volcanic zone (Fig. 1). Mutnovsky geothermal field (Fig. 2) with the installed capacity of power plants 62 MWe is important for the use of renewable energy sources in Kamchatka. Currently only one third of the geothermal field area is used (Fig. 2). Electricity and heat demand in Petropavlovsk-Kamchatsky and Yelizovo (~300 MW) make it economically feasible to consider further development of the Mutnovsky geothermal fields. The experience of Mutnovsky field exploitation may also be useful in the development of other large geothermal fields in the Kurile-Kamchatka region (Kiryukhin and Sugrobov, 2019).

The study of the Mutnovsky geothermal field in terms of the relationship between volcanic, hydrothermal and seismic activity is a related fundamental challenge. Large-scale exploitation of the Mutnovsky geothermal field since 2002 with fluid extraction up to 500 kg/s (600 MWh) is comparable to the average magma energy rate of two nearby active volcanoes Mutnovsky and Gorely (transport of thermal energy in magma over the lifetime of volcanoes). The increased phreatomagmatic activity of Mutnovsky volcano since 2000 may be related to the exploitation of geothermal fields.

After 40 years of dormancy, hydrothermal explosions and ash emissions occurred in the crater of Mutnovsky volcano in March 2000, April 2007 (Gavrilenko and Melnikov, 2008), May 2012, July 2013, February 2018, and spring 2020. Moreover, in 2010 there was a powerful vapor-gas eruption from the crater of Gorely volcano, its mass

---

* Corresponding author.
E-mail address: avkiryukhin2@mail.ru (A.V. Kiryukhin).

https://doi.org/10.1016/j.geothermics.2022.102474
Received 25 July 2021; Received in revised form 10 April 2022; Accepted 22 May 2022

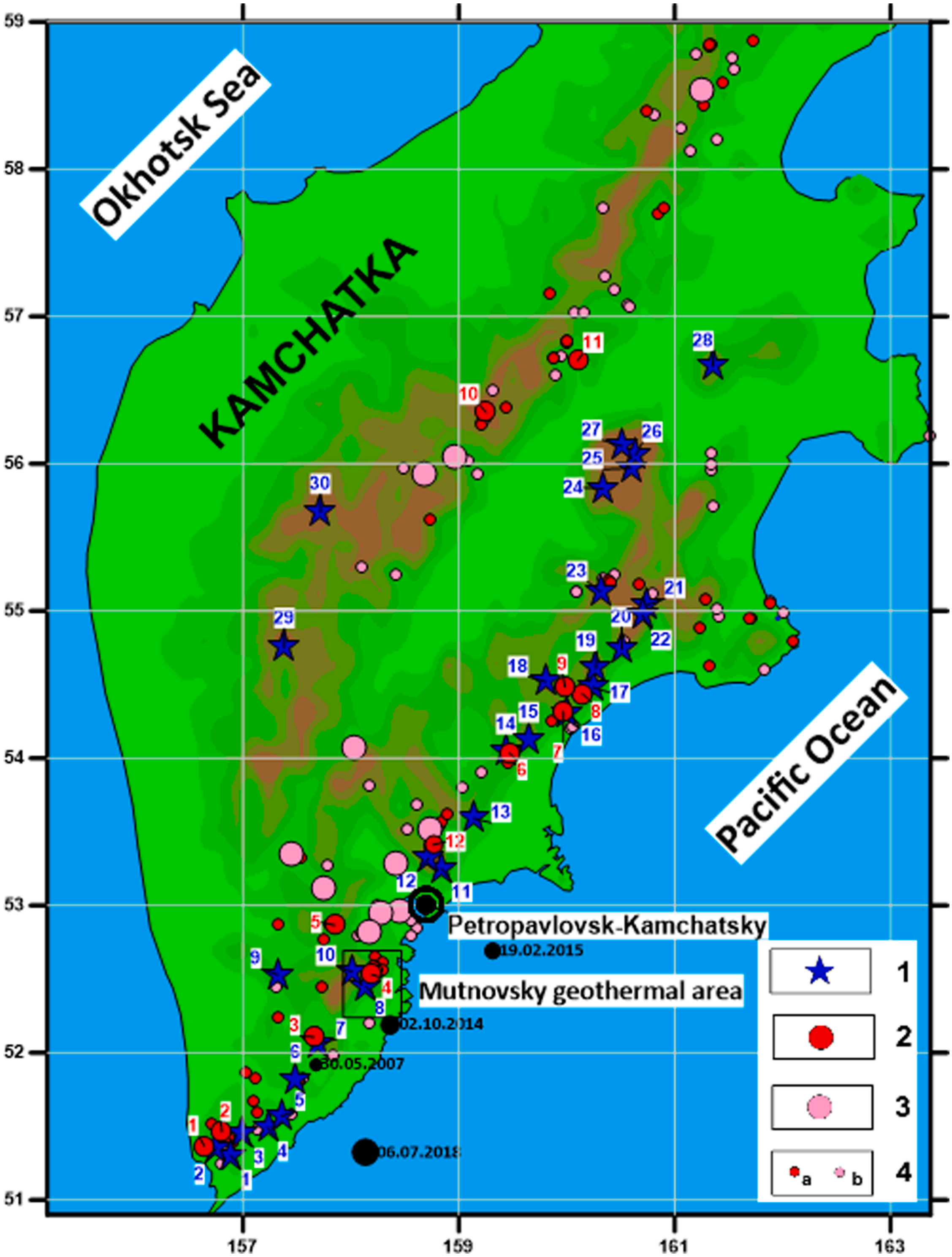

Fig. 1. Kamchatka volcanoes and HT fields, rectangle marks Mutnovsky geothermal area. Location map of the volcanoes and hydrothermal systems of Kamchatka, background color topo map used. 1—Active volcanoes (1, Kambalny; 2, Koshelevsky; 3, Diky Greben; 4, Ilynsky; 5, Zheltovsky; 6, Ksudach; 7, Asachinsky; 8, Mutnovsky; 9, Opala; 10, Gorely; 11, Avachinsky; 12, Koryaksky; 13, Zhupanovsky; 14, Karymsky; 15, Maly Semyachik; 16, Bolshoy Semyachik; 17, Kihpinych; 18, Taunshits; 19, Krasheninnikova; 20, Kronotsky; 21, Komarova; 22, Gamchen; 23, Kizimen; 24, Pl. Tolbachik; 25, Bezymyanny; 26, Kluchevskoy; 27, Ushkovsky; 28, Shiveluch; 29, Khangar; 30, Ichinsky); 2—High-temperature hydrothermal systems (1, Koshelevsky; 2, Pauzhetsky; 3, Hodutkinky; 4, Mutnovsky; 5, B-Banny; 6, Karymsky; 7, Semyachiksky; 8, Geyserny; 9, Uzonsky; 10, Apapelsky; 11, Kireunsky; 12, North-Koryaksky); 3—Hydrothermal systems with temperatures below 150 °C; 4—Groups of thermal springs: (a) temperature from 50 to 100 °C, (b) temperature from 20 to 50 °C. Filled black circles are regional earthquakes (data from KB FRC UGS RAS) discussed below in Section 5.2.

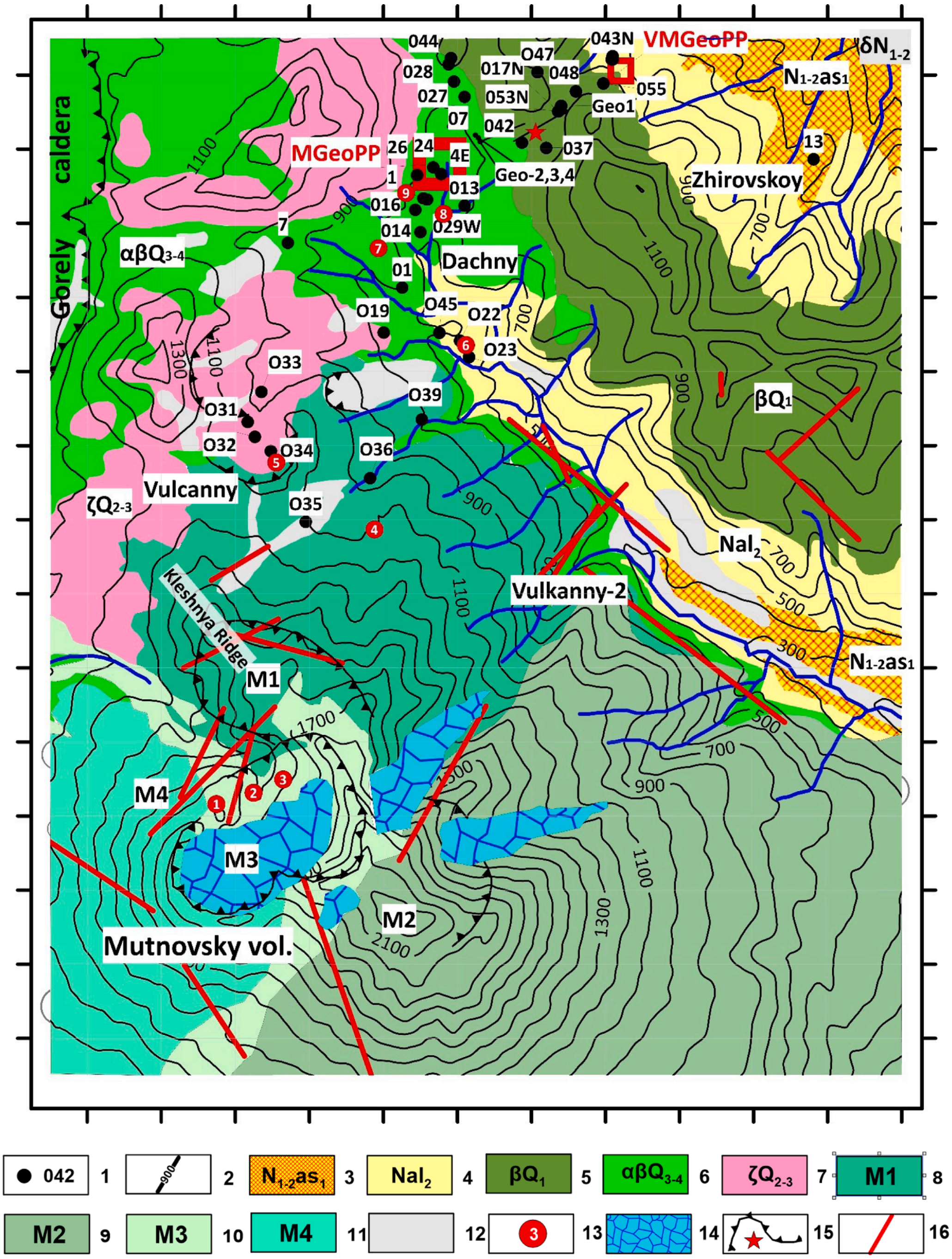

Fig. 2. Schematic geological map and topography of the Mutnovsky geothermal area. Map cover area from longitude of 158.13 E to 158.30 E and from latitude of 52.43 N to 52.56 N. Legend: 1 — wells; 2 — surface isolines, m; 3 - Miocene sandstones ($N_{1\text{-}2}as_1$) and diorite intrusions ($\delta N_{1\text{-}2}$); 4 — Pliocene lavas (Nal_2); 5 - Pliocene-Quaternary basalts and andesite tuffs and lavas (Zhirovskoy vol.) (βQ_1); 6 — Upper Pleistocene and Holocene andesites and basalts ($\alpha\beta Q_{3\text{-}4}$); 7 – Middle- and Upper Pleistocene rhyolite extrusions $\zeta Q_{2\text{-}3}$; 8,9,10,11 - M1, M2, M3, M4 – Mutnovsky-1, Mutnovsky-2, Mutnovsky-3 and Mutnovsky-4 volcanoes (by O.B. Selyangin, 1993); 12 - fluvio-glacial deposits (Q_4); 13— thermal features (see numbering below); 14 — glaciers in the crater of Mutnovsky volcanoes; 15 - volcano craters, funnels of phreatomagmatic explosions and magmatic rods; 16 - dykes traces at elevations of -500 m (see Fig. 4A and Section 2.1 for explanation). Other designations: MGeoPP - Mutnovskaya GeoPP 50 MWe; VMGeoPP - Verkhne-Mutnovskaya GeoPP 12 MWe; Dachny, Vulkanny, Vulkanny-2, Zhirovsky- potential sites for geoelectric power generation. Marking of the axes - 1 km. Thermal features (fumarole fields): 1 - Active crater; 2 - Bottom field; 3 - Upper field; 4, 5 - Severo-Mutnovsky (W and E); 6 - New 2003; 7 - Dachny (active group); 8 - Radon spring; 9 - Medvezhye.

flow rate is estimated at ∼130 kg/s (H_2O ∼ 93%, non-condensable gas (NCG) ∼7) (Aiuppa et al., 2012), the crater lakes of Mutnovsky and Gorely volcanoes were drained (in 2004 and 2012 respectively). Seismic activity has also increased; 568 earthquakes with ML-magnitudes above 1.0 (ML = Ks × 0.5 - 0.75 (Chubarova et al., 2010), where Ks is an estimate of the regional earthquakes from recordings of short-period seismometers (shear waves are used)) were recorded at depths above −10 km asl in Mutnovsky geothermal area (Fig. 2) from February 2009 to October 2020. Hydrothermal explosions and new boiling pots have occurred within the exploitation zone (thermal occurrence #6, Fig. 2), while the chloride hot springs of Voynovsky and Verkhne-Zhyrovsky have disappeared or degraded with a significant decrease in chlorine ion (Lower-Zhyrovsky).

This article deepens the understanding of the nature of seismic activity beneath Mutnovsky volcano as a result of magmatic injections beneath it (magmatic fracking), previously outlined in Kiryukhin et al. (2018). Including the possibility of aseismic injections (sills) corresponding to the formation of open fractures of hydrofracturing, conjugated with shear deformations (dykes) recorded from seismic data. Hydro-mechanical CFRAC modeling (the CFRAC program implements a system of equations of hydrodynamics, geomechanics and micro-earthquake conditions (McClure, 2012, 2014; McClure, Horne, 2013) is used to provide additional theoretical support for earthquake generation by injecting magma into existing shear fractures with low dip angles under horizontal compression (reverse-fault (RF)) geomechanical conditions. The time-varying 3D pattern of magmatic fracking is compared with the phreatomagmatic activity of Mutnovsky volcano and the inflow of magmatic gases into the productive geothermal reservoirs. The obtained information is also used to identify potential productive geothermal reservoirs in the northeastern sector of Mutnovsky volcano and to assess the possibility of increasing the electric capacity of Mutnovsky geoelectric power plants.

1.2. Geological stratification and Mutnovsky volcano productivity

The geological structure, hydrogeological conditions, and distribution of thermal characteristics in the Mutnovsky geothermal region are described in Vakin et al. (1986). The major geologic units in the Mutnovsky geothermal area that have been uncovered by wells or exposed at the surface include: (1) Miocene sandstone and Paleogene-Neogene volcano-sedimentary deposits; (2) Miocene diorite intrusions; (3) Pliocene dacite and rhyolite tuffs and lavas; (4) Pliocene-Quaternary basalts and andesite tuffs and lavas; (5) cones of volcanoes Mutnovsky-1, Mutnovsky-2, Mutnovsky-3, and Mutnovsky-4, respectively; (6) Upper Pleistocene and Holocene andesites and basalts; (7) extrusions of Upper Pleistocene rhyolites.

In the Mutnovsky productive reservoir, these geological units are defined as follows (Kiryukhin, 1993,1996): (1) Miocene sandstones ($N_{1-2}as_1$); (2) diorite intrusions (δN_{1-2}) (dykes penetrated by wells 04, 011, and 012); (3) Miocene intrusion contact zone (N_1br); (4) Miocene tuffs and lavas ($N_{1-2}as_2$); (5) rhyolite Pliocene tuffs (Nal_1); (6) Pliocene lavas (Nal_2); (7) Quaternary ignimbrites, tuffs and lavas, rhyolite-dacite extrusions.

Mutnovsky volcano is a complex of four volcanic cones (M1, M2, M3, and M4) that have been consistently active since the Late Pleistocene (Fig. 2). The geology of the area has been studied in detail and summarized in Selyangin (1993, 2009) and Simon et al. (2014) as follows. Mutnovsky-1 volcano (the oldest of the four) was active 60–80 thousand years ago. Mutnovsky-1 formed basaltic, andesite-basaltic, andesite and dacite lavas and pyroclastic rocks with a total volume of about 58 km3. At present, in the outcrops of the northeastern sector of the Kleshnya Ridge, a complex of basaltic dykes of submeridional strike, which are considered as an eroded part of the feeding magmatic system of the Mutnovsky-1 volcano, can be seen. Volc. Mutnovsky-2 functioned 30–40 thousand years ago, its center was located 3 km southeast from the center of Mutnovsky-1, Mutnovsky-2 erupted about 24 km3 of lava and pyroclastics. The composition of the volcanic rocks of Mutnovsky-2 varies from basaltic to dacite and is generally similar to that of Mutnovsky-1. Mutnovsky-3 is located between Mutnovsky-1 and Mutnovsky-2. Mutnovsky-3 is located between Mutnovsky-1 and Mutnovsky-2 (Fig. 2) and has a relatively small volume of volcanic rocks (~5 km3). Mutnovsky-3 is composed of alternating lava and pyroclastic flows with parasitic cones on the periphery, which is also characteristic of Mutnovsky-1 and Mutnovsky-2 volcanoes. Mutnovsky-3 is permeated by basalt dykes, and its central part is composed of hydrothermally altered rocks. The composition of volcanic rocks in Mutnovsky-3 varies from basaltic to rhyodacite. The summit caldera of Mutnovsky-3 is 1.5 × 2.0 km (Fig. 2), it was formed by the eruption of 2.0–2.5 km^3 of pumice and is currently partially filled with glacier (2.5 km^2) and lava flows from Mutnovsky-4. Mutnovsky-3 also contains an intracaldera basalt-andesite cone and rhyodacite extrusion. The end of the Mutnovsky-3 activity is fixed by the extrusion of a dacite dome, the age of which is estimated by local tephrostratigraphy to be about 4000 years (Selyangin, 1993; Simon et al., 2014).

Petrological studies and modeling (Simon et al., 2014) indicate that the Mutnovsky dacites are a product of partial melting of the preceding amphibole-bearing basaltic magmas under crustal medium-temperature and baric conditions. Mutnovsky-4 is the youngest volcano in the Mutnovsky volcano complex, with an estimated age of about 11 thousand years (Selyangin, 1993). Mutnovsky-4 is located 1 km to the SSW of Mutnovsky-3, its total volume is estimated at 3.8 km^3. Mutnovsky-4 is composed of lavas and pyroclastic flows of andesibasaltic composition. Thus, the activity mode of Mutnovsky volcano during the last 30 thousand years has significantly changed from effusive-pyroclastic to magmatic.

1.3. Reservoir thermal-permeability and surface discharge distributions

The results of exploration drilling in the Mutnovsky geothermal area revealed three high-temperature geothermal reservoirs with temperatures above 220 °C at −250 m (Dachny, Vulkanny and Verkhne-Zhirovskoy sites) (Asaulov et al., 1987). The positioning of these reservoirs coincides with the NNE striking zone, starting from Mutnovsky volcano (Vakin et al., 1986). The thermoanomaly of the most heated Dachny geothermal reservoir is characterized by temperatures in the 220–260 °C range at −250 m; this thermoanomaly has an asymmetric shape in the meridional section, indicating upward flow conditions with temperatures above 300 °C from the south. The lateral temperature distribution indicates sublateral flows from the Dachny reservoir northeastward to the Verkhne-Mutnovsky steam jets and Voinovsky hot springs, as well as the possibility of sublateral flow from the Verkhne-Zhirovsky reservoir to the Nizhne-Zhirovsky and Vilyuchinsky hot springs (in addition to Fig. 2, see also Fig. 1 in Kiryukhin et al., 2018). Sublateral flows identified by the peculiarities of temperature distribution may also exist in the reservoir and near contact systems of Miocene dacite and rhyolite tuffs and lavas hydraulically connected by the system of productive faults indicated below.

The productive faults (plane-oriented clusters of productive zones and zones of total loss of circulation) for the Mutnovsky geothermal reservoir (Kiryukhin et al., 2018) include the productive fault "Main" (dip angle 60.4°, dip azimuth 106° to SE, extending to NE) in the Dachny site and the productive fault "North-East" identified in the Verkhne-Mutnovsky site (dip angle 60° SE). 3D views of production faults are presented in Section 2.1 below (Figs. 5A, 5B and 5C).

We should also point out the very low piezometric initial water level in the productive geothermal reservoirs, which reaches 500–600 m below the ground surface in the Dachny site and 600–700 m in the Vulkanny site. This is reflected deep seated two-phase conditions are formed in the upper parts of the high-temperature geothermal reservoirs, and the pressure distribution is determined by the temperature distribution of the host rocks.

2. Magma activity of Mutnovsky volcano

2.1. Magma fracs based on seismicity data

Let's now proceed to the analysis of the current seismic activity of the Mutnovsky volcano (assumed to be closely related to its magmatic activity) according to seismic data 2009–2020. Five seismic stations can record seismicity in the Mutnovsky-Gorely volcanic cluster (MTV, GRL, ASA, RUS, PET, see Fig. 1 in: Kiryukhin et al., 2018). Identification of dykes and sills was carried out according to the micro-earthquakes (MEQ) catalogs of the KB FIC UGS RAS (2009–2020), using the Frac-Digger program (Kiryukhin and Kiryukhin, 2016) with sampling criteria ($\delta_t = 30$ days, $\delta_R = 6$ km, $\delta_Z = 1$ km, $N = 6$). A full description of Frac-Digger workflow was given in Section 2.2 of the paper Kiryukhin et al., 2016 and most important features are also given in Appendix B. Additional testing of magma fracking events estimates using the most reliable hypocenters data (Zemletryaseniya Rossii v 2009g. (Earthquakes in Russia in the year 2009), Obninsk: GS RAN, 2009… Zemletryaseniya Rossii v 2019g. (Earthquakes in Russia in the year 2019), Obninsk: GS RAN, 2019) were done (see Appendix C). Between January 2009 and October 2020, 2122 earthquakes were recorded in the Mutnovsky geothermal area, 76% of them constituting 116 plane-oriented clusters (including 105 associated with the Mutnovsky volcano), interpreted as dyke injections.

The spatial characteristics of the dyke complex are as follows (Figs. 3, 4): 1. Most of the dykes were injected in the northeastern sector of Mutnovsky volcano over an area of 2 × 10 km. 2. Most of the dykes beneath Mutnovsky volcano have a dip angle of 20 to 40° 3. Most of the dykes were injected at a depth of −4.0 to −2.0 km with a NE-SW (20–50°) strike. 4. Eleven dykes were injected near the southeastern

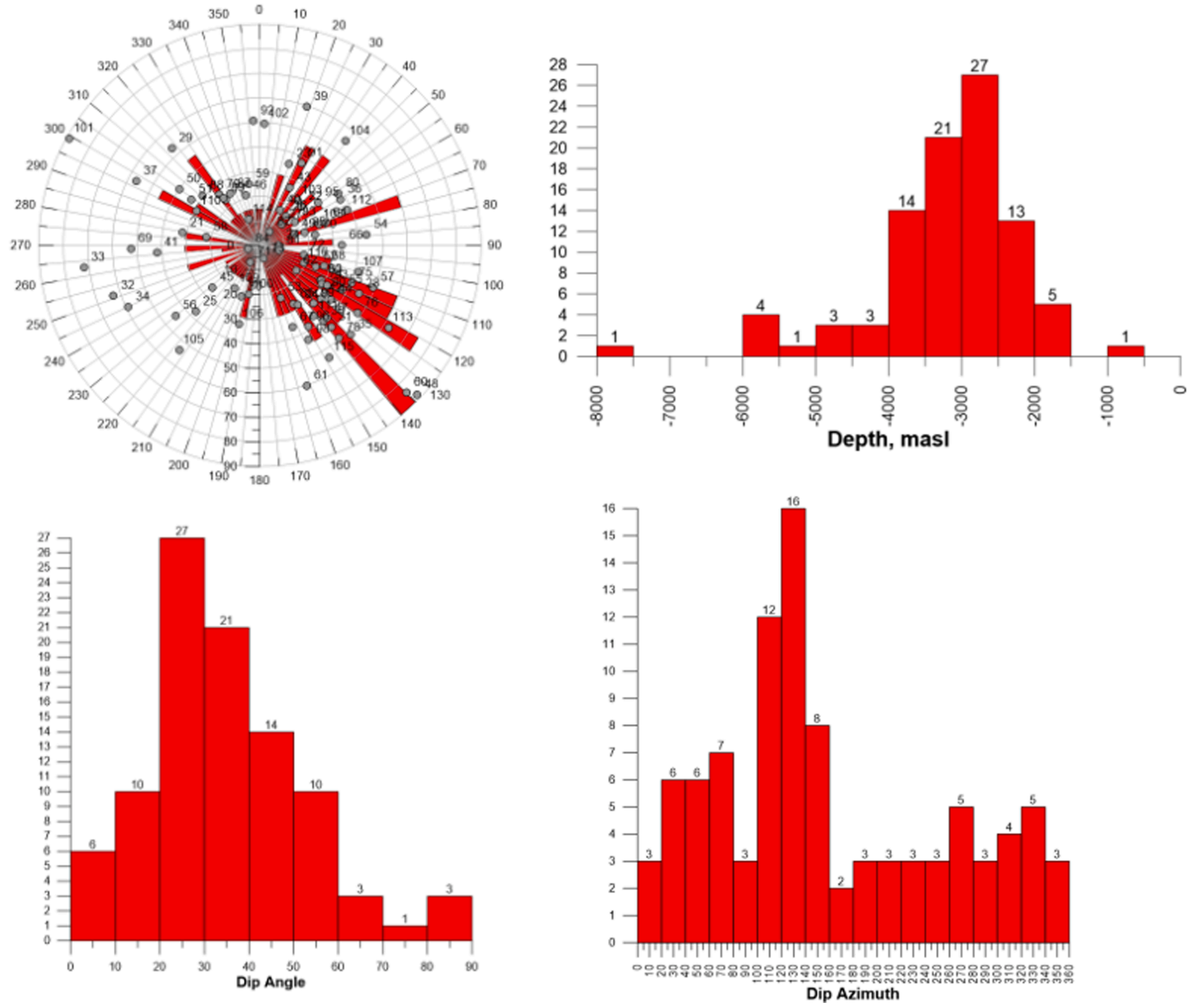

Fig. 3. Stereogram and histograms of the distribution of plane-oriented clusters of earthquakes (dip angle, dip azimuth, depth). The data were obtained from the processing of seismic data KB FIC UGS RAS of the Mutnovsky volcano (2009–2020) using the Frac-Digger program. Prevalence of dykes of dykes with a 30° dip angle and NNE strike indicate geomechanical conditions of RF horizontal compression in the NWW direction.

boundary of the Mutnovsky produced geothermal reservoir at a depth of −6.0 to −4.0 km 5. Magnitudes (ML=Ks×0.5–0.75, Chubarova et al., 2010) of seismic events during dyke injections ranged from −0.1 to 2.85. 6. We observe a trend towards an increase in the dip angle of the dykes northward from Mutnovsky volcano (1°/km).

Some features of dyke system injections distributions are shown on Fig. 4 at different elevations of −500, −1500 and −3000 m, correspondingly, and in Table 1. At elevation of −500 m shown on Fig. 4A one can see: (1) Traces of dykes 96, 98, 106 in a close vicinity of blowing well 035; (2) Traces of dykes 34, 48, 101, 104, 105 precisely following topo-hydrographic features in mid-stream of Falshivaya river; (3) Swarm of dykes (12, 18, 28, 32, 35, 80, 107) beneath active fumarole fields in Mutnovsky volcano craters (shown as thermal features 1, 2, 3 on Fig. 2). At elevation of −1500 m, shown on Fig. 4B one can see similar features: (1) Traces of dykes 86, 96, 98, 107 in a south vicinity of blowing well 035; (2) Traces of dykes 25, 29, 34, 41, 48, 56, 69, 101, 104, 105, 113 precisely following topo-hydrographic features in mid-stream of Falshivaya river; (3) Swarm of dykes (12, 18, 20, 28, 30, 32, 33, 50, 55, 64, 66, 68, 75, 78, 80, 91, 92, 102, 106, 112) beneath active fumarole fields in Mutnovsky volcano craters. At elevation of −3000 m a number of dyke traces significantly increased (Fig. 4C), forming a most concentrated area beneath thermally active craters of Mutnovsky volcano and in northeast sector of Mutnovsky volcano, the total area of detected dyke traces at this elevation accounted as 62 km^2.

The geometry of injection dykes in the vicinity of the Mutnovsky volcano reflects the geomechanical conditions of reverse faults (RF): SH max > Sh min > Sv, and indicates the orientation of SH max in the SE direction. Thus, we can suggest a magma feeding sub-horizontal open mode fractures (sills derived from Mutnovsky volcano magma recharge channel) for shear mode low angles dyke system. The most probable elevation range for sills injections is from −3500 to −2500 m beneath Mutnovsky volcano. Open mode fracturing is silent from seismic point of view, so we can't detect sills injections using seismic data, like shear mode fractures done. Figs. 5A and 5B shows 3D view of suggested sill position and featured dykes injected around well 035 (Fig. 5A) and beneath mid-stream of Falshivaya river (Fig. 5B), as discussed above. Fig. 5C shows dykes injections followed by magma gas release in production geothermal reservoir, reflected by P_{NCG} excursions in

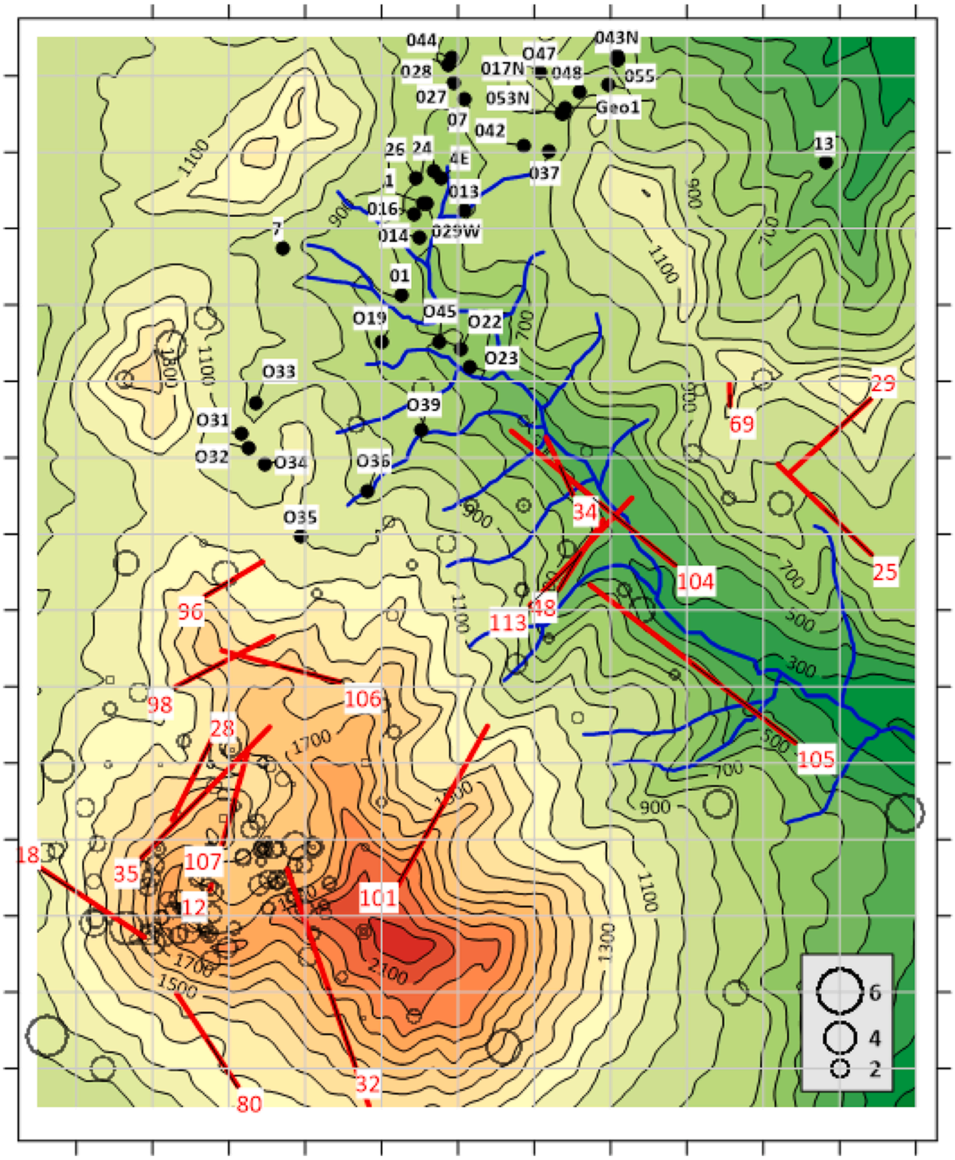

Fig. 4A. Schematic topo map and dyke traces of Mutnovsky geothermal area. Legend: dykes traces at elevations of −500 m are shown by red lines with numbers (see Table 1), wells are shown by black filled circles with numbers, MEQ's epicenters (projected from hypocenters in a range of depth from –1500 to 500 m) are shown by empty circles proportional to MEQ's magnitudes (scale is in Ks), Falshivaya river is shown by blue lines. Axes scale – 1 km, map coverage is the same as Fig. 2.

Table 1

Magmatic injection (planar MEQ cluster) patterns. This table shows characteristics of the approximation planes of plane oriented clusters of MEQ's, interpreted as dykes discussed above and shown in Figs. 4 and 10 (as a dyke traces) and in Fig. 5 (as 2D convex polygons in 3D space).

Claster ##	Dip angle (deg)	Dip Azimuth (deg)	X m	Y m	Z m	Date	ML	Number of events	Area, km^2
12	50	111	44,559	14,111	−2610	08.11.13	1.55	7	14.4
18	48.1	34	42,226	15,135	−2016	20.03.14	1.85	13	15.1
20	27.9	93	42,230	14,064	−1769	03.04.14	1.25	11	10.0
25	37.5	224	48,149	17,837	−2738	28.05.14	1.4	13	20.2
27	12.3	46.3	44,703	14,350	−3000	20.06.14	1.6	36	17.3
28	44.8	116	44,222	15,215	−2273	23.06.14	1.3	7	20.7
29	53.4	318	49,080	23,732	−5566	14.07.14	2	16	27.3
30	28.4	120	44,731	15,370	−2603	17.07.14	1.45	60	20.4
32	63	251	43,038	13,693	−2438	25.07.14	1.85	25	21.6
33	72.2	263	42,328	15,729	−4798	31.07.14	1.4	10	22.9
34	59.1	245	44,760	20,105	−4229	07.08.14	2	6	18.4
35	51.9	134	44,238	14,871	−2574	21.08.14	1.45	20	18.5
41	41.9	266	46,807	17,817	−2947	19.02.15	1.4	11	20.5
48	88.3	134	48,593	18,758	−24,669	29.05.15	3.05	6	212.4
50	39.9	305	43,843	16,141	−1796	08.08.15	1.6	13	8.7
52	24.5	110.9	45,376	15,252	−2636	30.08.15	1.25	54	17.0
55	37.9	119	45,671	15,871	−2722	07.10.15	1.3	15	17.9
56	44.6	230	49,135	17,640	−2425	11.10.15	1.8	7	20.1
62	18	124.9	44,353	15,129	−3286	31.03.16	1.45	32	20.2
64	28.2	71	42,486	13,772	−1715	04.04.16	1.35	8	9.1
66	33.4	90	43,982	14,774	−2613	05.05.16	1.15	32	13.1
68	27.5	108	44,361	15,037	−2944	26.05.16	1.9	23	15.0
69	52.5	269	47,606	18,853	−3116	18.06.16	1.35	6	7.9
75	40.3	112	45,141	14,758	−2779	05.10.16	1.55	9	6.0
78	49.6	139	45,222	16,133	−2846	15.05.17	1.55	8	14.2
80	38.3	57	43,455	14,746	−2017	07.09.17	2.3	14	15.1
86	22.2	200	44,474	14,797	−2887	21.02.18	1.7	6	15.7
91	37.6	27	43,163	14,870	−2234	11.06.18	1.8	15	7.6
92	50.7	357	42,579	16,113	−2629	01.07.18	1.2	6	11.5
96	38.5	149	44,866	16,441	−2585	21.04.19	1.95	7	15.5
98	43.1	153	43,645	16,022	−1889	21.08.19	1.5	7	10.9
100	20.4	192	42,293	16,144	−2421	10.04.20	1	8	6.8
101	88.8	299	45,238	15,263	−19,803	26.04.20	3.15	9	216.7
102	49.5	2	42,873	15,813	−2296	13.05.20	1.45	54	20.9
103	23.9	40	44,315	15,166	−2727	20.05.20	1.2	90	18.2
104	54.9	39	47,853	19,518	−625	25.05.20	2.05	8	10.2
105	53.7	218	47,455	16,627	−2566	04.06.20	1.45	7	15.6
106	33.1	195	43,375	15,520	−1651	10.06.20	1.55	23	13.3
107	41.6	105	44,908	15,627	−2045	23.06.20	1.65	15	21.8
108	25.5	70.4	44,794	15,076	−3604	13.07.20	1.1	32	14.9
109	20.3	211	43,147	14,294	−2657	25.07.20	1.2	7	1.0
110	29.3	298	46,193	18,452	−2954	22.08.20	1.8	27	16.3
111	36.1	142.5	45,603	15,847	−3168	25.08.20	1.35	46	17.6
112	38.3	68	44,586	14,989	−2596	11.09.20	1.5	9	14.8
113	62.1	123	47,664	17,339	−2002	13.09.20	1.6	7	7.8
114	11.6	336	45,417	23,347	−5906	30.09.20	2.45	6	8.8
115	53.6	148	44,210	15,760	−2483	16.10.20	1.35	8	10.7
116	19.2	111.8	43,930	15,026	−2747	01.12.20	1.3	83	9.7

Note 1: ML=Ks×0.5–0.75.

Note 2: 2D polygons were derived from approximation planes of plane oriented clusters of MEQ's hypocenters. To do this, Frac-Digger program put projections of MEQ's hypocenters into approximation plane, then search convex polygon which included projection points (that is one of 2D polygons was shown in a Fig. 5). Red lines in Fig. 4 are intersections of the 2D polygons above mentioned with horizontal planes at defined levels (Fig. 4A at $z = 500$ m, Fig. 4B at $z=-1500$ m, Fig. 4C at $z=-3000$ m).

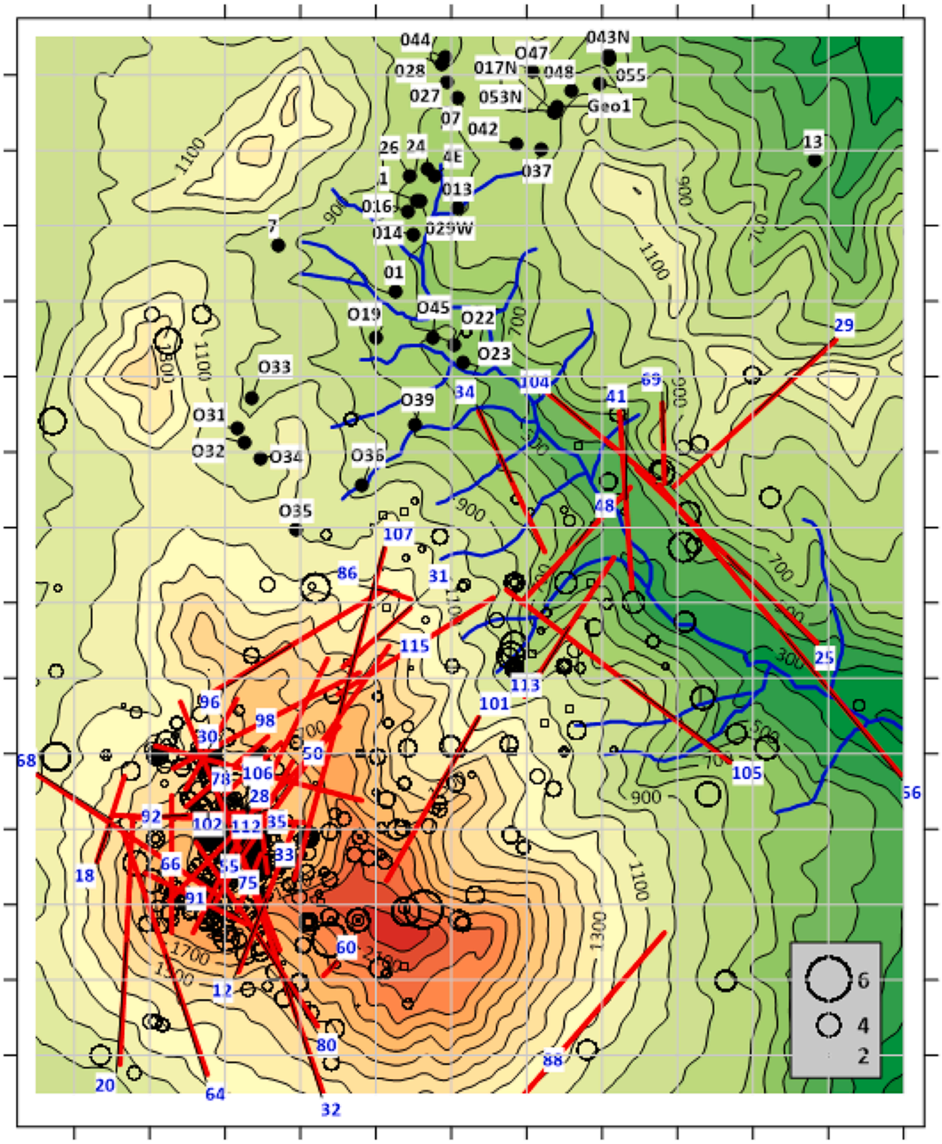

Fig. 4B. Schematic topo map and dyke traces of Mutnovsky geothermal area. Legend: dykes traces at elevations of −1500 m are shown by red lines with numbers (see Table 1), wells are shown by black filled circles with numbers, MEQ's epicenters (projected from hypocenters in a range of depth from –2500 to −500 m) are shown by empty circles proportional to MEQ's magnitudes (scale is in Ks), Falshivaya river is shown by blue lines. Axes scale – 1 km, map coverage is the same as Fig. 2.

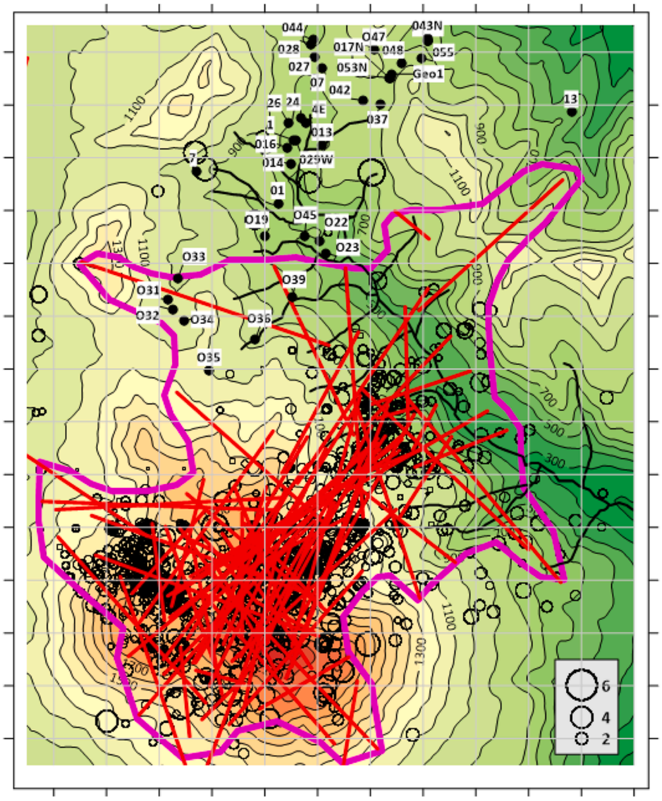

Fig. 4C. Schematic topo map of Mutnovsky geothermal area. Legend: dykes traces at elevations of −3000 m are shown by red lines, main feeding sill contours at elevation of −3000 m is shown by magenta thick line, wells are shown by black filled circles with numbers, MEQ's epicenters (suggested from hypocenters in a range of depth from –4000 to −2000 m) are shown by empty circles proportional to MEQ's magnitudes (scale is in Ks), Falshivaya river is shown by blue lines. Axes scale – 1 km, map coverage is the same as Fig. 2.

Mutnovsky GeoPP, which is discussed below in Section 3.

2.2. CFRAC hydro-mechanical modeling of magma injection (dyke case)

2.2.1. Model setup

Based on seismic data, let us consider a conceptual model of hydromechanical processes beneath Mutnovsky volcano. We consider a single existing fault in RF geomechanical conditions as the host fault for the injecting dyke (Fig. 6) and apply CFRAC modeling to describe magma injection into it (McClure and Horne, 2013; McClure, 2014; Kiryukhin and Norbeck, 2017). For the indicated geomechanical conditions, the vertical stress Sv is the minimum, the maximum horizontal stress SH max acts in the NW direction, and the minimum horizontal stress Sh min acts in the NE direction. At a depth of z0 = 4500 m (≈ −3000 m), Sv is estimated as 113 MPa (Eq. (A1), Appendix (Stresses Estimations)); SH max = 279 MPa (Eq. (A2), Appendix (Stresses Estimations, where Pp = Pf = 35 MPa fluid pressure at −3000 m, friction coefficient μ = 0.6); Sh min - is taken equal to (Sv + SH max)/2 = 196 MPa.

Based on the above, the effective stress tensor under Mutnovsky volcano at a depth of −3000 m in the coordinate system oriented along the main stress directions X, Y, Z (X - SE direction, Y - NE direction, Z - upward direction, see Fig. 6) is written as follows:

$$\sigma_g = \begin{pmatrix} SH\max - Pf & 0 & 0 \\ 0 & Sh\min - Pf & 0 \\ 0 & 0 & Sv - Pf \end{pmatrix}, \qquad (1)$$

where SH max = 279 MPa, Sh min = 196 MPa, Sv = 113 MPa, Pf = 35 MPa.

The CFRAC program solves a system of hydro-mechanical equations describing flows and deformations in a network of discrete fracture system (McClure, 2014; McClure and Horne, 2013). A double iteration scheme is used in CFRAC, in which the equation for flow is combined with the condition for normal stresses, and shear stresses in the fracture plane form a second system of equations for quasi-static equilibrium conditions. When performing 3D modeling using CFRAC software, the following should be kept in mind: (1) CFRAC in the basic version describes processes in vertical fractures; (2) when describing inclined fractures, it is necessary to rotate the original XYZ coordinate system around the Y axis into a new coordinate system with the Z2 axis in the fracture plane (Y2 = Y); (3) after that, the effective stresses in the new coordinate system X2, Y2, Z2: σ_{xx}, σ_{yy}, σ_{zz}, σ_{xz} and their trends should be redefined.

The CFRAC program defines the threshold values of shear strain rates for earthquake generation as 5 and 2.5 mm/s, respectively (default values of the meqstartvel and meqendvel parameters). At this point, the model element in which the specified condition is reached is interpreted as the initial rupture point, which ends when the shear strain rate falls below the threshold value. Earthquake parameters are identified as follows within the CFRAC program: time, hypocenter coordinates, seismic moments and magnitudes, and rupture areas, and are written to

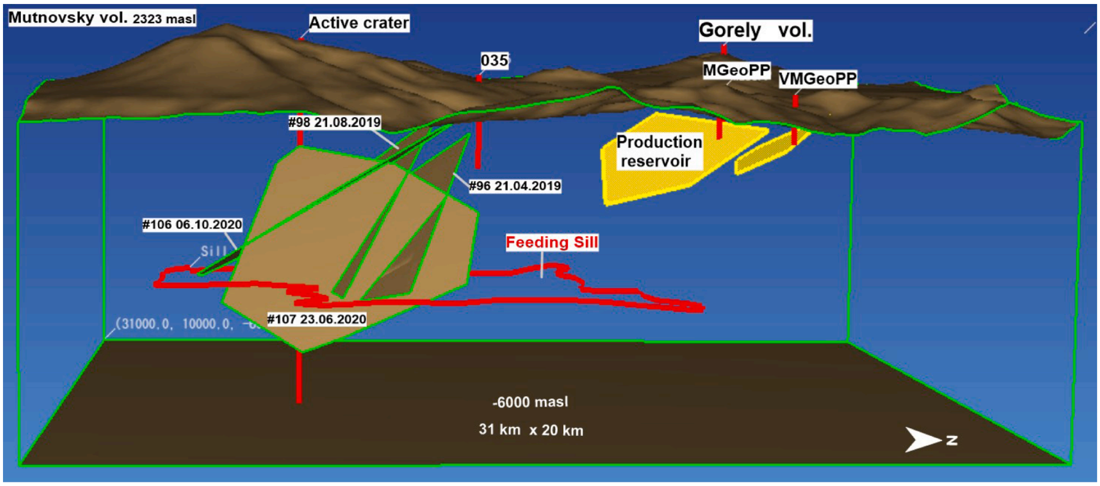

Fig. 5A. 3D view of the feeding sill and selected dyke injections 2019–2020 beneath Mutnovsky volcano, dykes directed around to well 035. Dykes shown are: 96, 98, 106, 107 (see Table 1). Production reservoir faults are shown by highlighted polygons too.

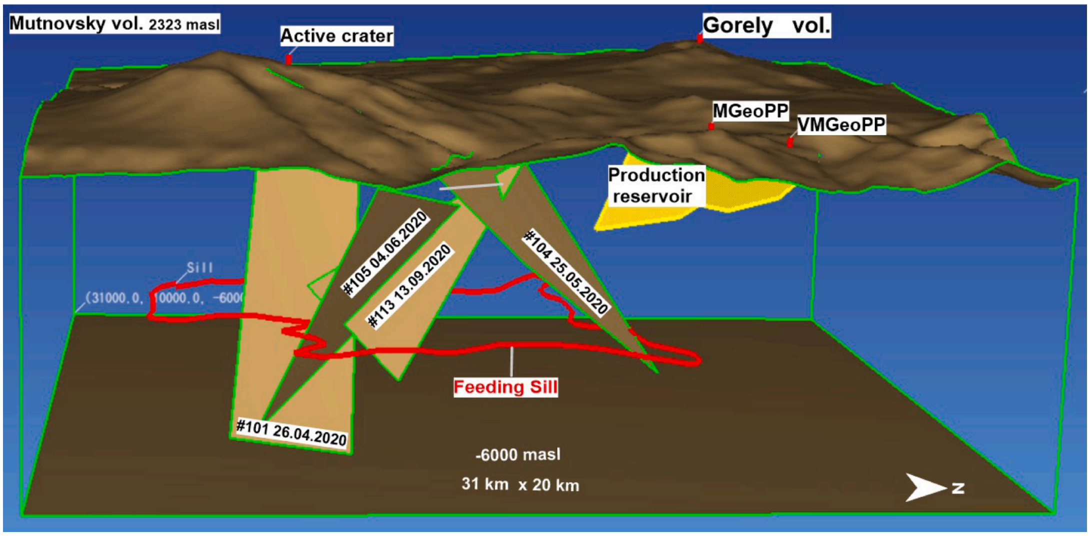

Fig. 5B. 3D view of the feeding sill and selected dyke injections in 2020 traced above −500 m in northeast sector beneath Mutnovsky volcano (a new promising geothermal production area in Falshivaya river basin). Dykes shown are: 101, 104, 105, 113 (see Table 1). Production reservoir faults are shown by highlighted polygons too.

the resulting files.

The seismic moment in CFRAC program M0 is estimated from the shear strain data as follows: $M0 = G \times \int \text{slip}\, dA$, where G - shear modulus, A - shear area. Then the magnitude Mw is calculated:

$$Mw = log(M0)/1.5 - 6.06 \tag{2}$$

- where M0 is expressed in N × m. In the considered model the static/dynamic option was used: friction coefficient μstatic = 0.6 in absence of rupture, at the beginning of rupture deformation the friction coefficient drops to μdynamic = 0.55 (friction coefficients values were assigned accordingly to McClure (pers. com., 2017), while we understand uncertainty of μstatic/μdynamic model parameter, and treat this as estimated parameter, varying μdynamic in a range from 0.55 to 0.599 (Table 3)). In the considered basic modeling scenario, magma injection occurs in a fracture with a dip angle of 30° and dimensions of 4 km (in the dip direction) by 4 km (in the strike direction) with the center of the fracture at a depth of 4500 m (or - 3000 m) under the Mutnovsky volcano. In addition, the modeling assumed the following conditions: duration of magma injection from 1 to 30 days, magma flow rate from 10 to 2000 kg/s, maximum pressure during injection 200 MPa (CFRAC upper limit). Physical properties of magma: density 2800 kg/m3, viscosity was set from $9\ 10^{-5}$ Pa × s (basalt magma) to 2 Pa × s (andesite magma). Initial magma pressure was set from 5 to 78 MPa, the latter value corresponds to the fluid pressure necessary to activate the fracture according to the Mohr diagram (Fig. 4.18, Kiryukhin, 2020). In addition, other additional scenarios were considered on the model, with the parameters specified in Tables 2 and 3.

Worth noting, duration of magma injection from 1 to 30 days, magma flow rate from 10 to 2000 kg/s – are reasonable range of values to fit. For example, duration of magma injections/seismic activity before volcano erupt was 2 days before eruption 2012 of Tolbachik volcano (p.280, Table, Kiryukhin et al., 2016)) and average volcanoes magmatic injection rates were estimated from 3 to 111 kg/s for Kluchevskoy Group of Volcanoes during time period from 2000 to 2017 (Table 1, Kiryukhin et al., 2018). Uncertainties of magma injection duration and rate were analyzed using various modeling scenarios.

The effective stress tensor in the dyke-fracture coordinate system (X2

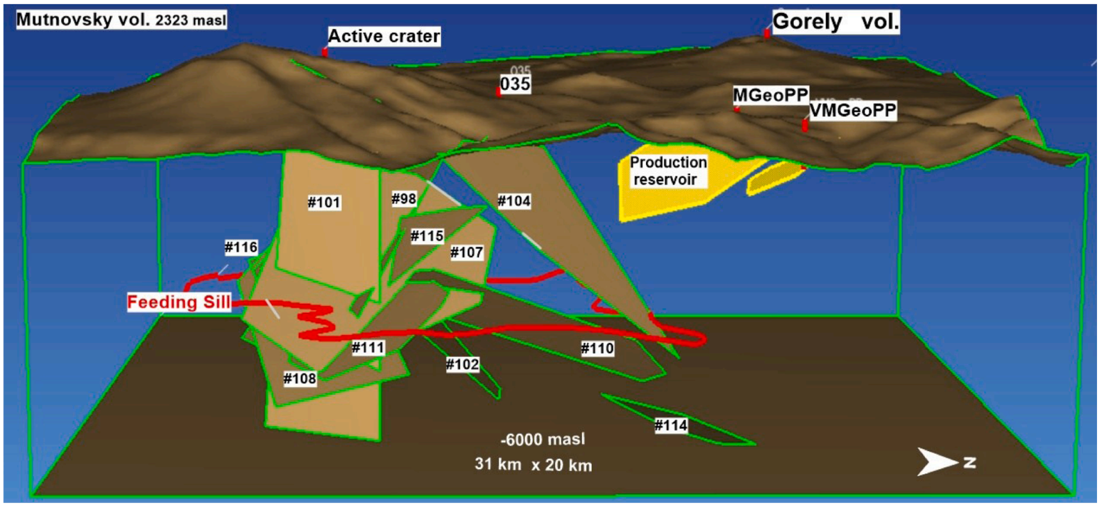

Fig. 5C. 3D view of the feeding sill and selected dyke injections in 2019–2020 possibly reflected in P_{NCG} excursions at Mutnovsky GeoPP (see below in Section 3). Dykes shown are: 98, 101, 102, 104, 107, 108, 110, 111, 114, 115, 116 (see Table 1). Production reservoir faults are shown by highlighted polygons too.

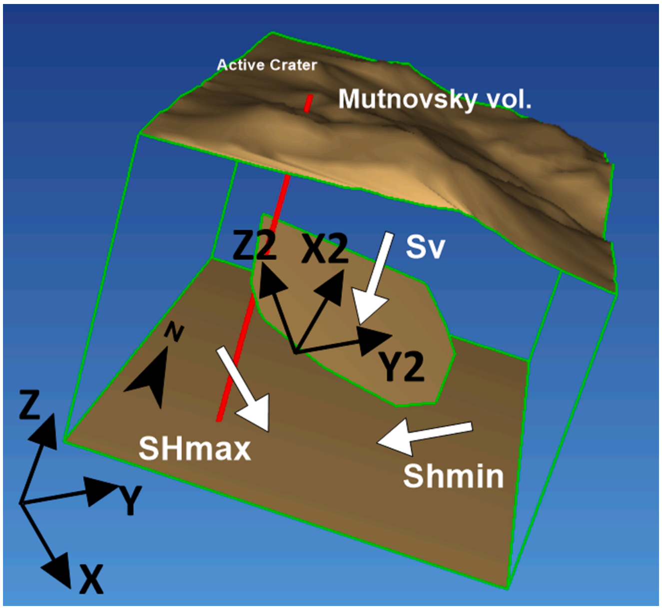

Fig. 6. A conceptual model of the geomechanical state during dyke injection beneath Mutnovsky volcano. Sv - vertical stress, SH max - maximum horizontal stress, Sh min - minimum horizontal stress.

- rotation of the X axis around the Y axis by an angle β = 60°, Y2 = Y) was calculated (in MPa) using the known effective stress tensor in the main stress coordinate system (1) and the coordinate transformation matrix:

$$A = \begin{pmatrix} \cos(\beta)\cdot\cos(\alpha) & -\cos(\beta)\cdot\cos(\alpha) & -\sin(\beta) \\ \sin(\alpha) & \cos(\alpha) & 0 \\ \sin(\beta)\cdot\cos(\alpha) & -\sin(\beta)\cdot\cos(\alpha) & \cos(\beta) \end{pmatrix}, \tag{3}$$

where α is the strike azimuth (for the coordinate system of main stresses α = 0).

Accordingly, effective stress tensor:

$$\sigma_f = A\cdot\sigma_g\cdot A^T, \tag{4}$$

where A^T — transposed matrix A. As a result, σ_f is equal:

$$\sigma_f = \begin{pmatrix} 119.8 & 0 & 71.9 \\ 0 & 161.3 & 0 \\ 71.9 & 0 & 202.8 \end{pmatrix}, \tag{5}$$

Since gravity is not directly considered in CFRAC, the stress trends in the fracture-dyke coordinate system must be determined: $\frac{\partial\sigma_{xx}}{\partial z} = 12.4$ MPa/km, $\frac{\partial\sigma_{yy}}{\partial z} = 16.7$ MPa/km, $\frac{\partial\sigma_{zz}}{\partial z} = 21.0$ MPa/km, $\frac{\partial\sigma_{xz}}{\partial z} = 7.4$ MPa/km. The above stress trends were calculated by numerical differentiation of the stress tensor, using ΔZ increments and assuming that the effective stress in the host rock masses is controlled by hydrostatic water pressure.

Table 2
Basic CFRAC modeling parameters and their values.

Parameter	Value	Dimension
S_v	113	MPa
$S_{H\ \max}$	279	MPa
$S_{h\ \min}$	196	MPa
µstatic friction coefficient	0.6	
µdynamic friction coefficient	0.55–0.599	
Shear modulus	1500 - 150,000	MPa
Poisson's ratio	0.25	
Eo (eo=Eo/10) fracture void aperture	0.0005–1.0	m
Magma viscosity	from 9 × 10^{-5} to 2	Pa•s
Magma density	2800	kg/m^3
Pf, water pressure	35	MPa
P init, initial magma pressure	5–78	MPa
Maximum injection pressure	200	MPa
Magma rate	10–2000	kg/s
Injection duration time	1–30	day
Fracture spaceing	4 × 4, 2 × 2, 0.2 × 0.2	km

Notes: Stresses and pressures are considered in the coordinate system of the main stresses at a depth of −3000 m.

Table 3
CFRAC modeling scenarios. Note: Mo, seismic moment (or E –energy) was calcualated using relationship (2).

##	Rate, kg/s	µ, Pa×s	P init MPa	G MPa	Area km^2	µu stat	µu dyn	E, m	Time, days	N	Mw max	M_0 N×m (J)
1	100	2	78	15,000	4 × 4	0.6	0.55	0.01	30	545	4.98	1.39E18
2	100	2	78	15,000	4 × 4	0.6	0.55	0.1	30	155	4.99	1.40E18
3	100	2	78	15,000	4 × 4	0.6	0.55	1.0	30	119	4.94	1.28E18
4	10	2	78	15,000	4 × 4	0.6	0.55	1.0	30	89	4.93	9.74E17
5	10	2	10	15,000	4 × 4	0.6	0.55	1.0	30	32	5.01	2.93E17
6	10	2	5	15,000	4 × 4	0.6	0.55	1.0	30	31	5.00	2.39E17
7	10	2	20	15,000	4 × 4	0.6	0.55	1.0	30	28	4.91	3.33E17
8	100	2	78	1500	4 × 4	0.6	0.55	0.01	30	833	4.84	5.23E17
9	10	2	78	150,000	4 × 4	0.6	0.55	1.0	30	79	4.93	9.74E17
10	**2000**	**9e-5**	**78**	**15,000**	**4 × 4**	**0.60**	**0.59**	**0.0005**	**1**	**7318**	**4.07**	**7.3E16**
11	2000	9e-5	78	15,000	4 × 4	0.60	0.599	0.0005	1	20,848	3.64	5.18E16
12	200	9e-5	78	15,000	4 × 4	0.60	0.595	0.0005	1	3196	4.11	4.70E16
13	2000	9e-5	78	1500	4 × 4	0.60	0.59	0.0005	1	7153	4.07	7.41E16
14	2000	9e-6	78	15,000	4 × 4	0.60	0.59	0.0005	1	8738	4.09	9.08E16
A1	2000	9e-5	10	15,000	4 × 4	0.60	0.59	0.0005	1	12,316	4.48	3.00E17
A2	2000	9e-5	10	15,000	2 × 2	0.60	0.59	0.0005	1	58	3.72	1.39E15
A3	2000	9e-5	10	15,000	0.2 x 0.2	0.60	0.59	0.0005	1	55	3.51	5.32E14

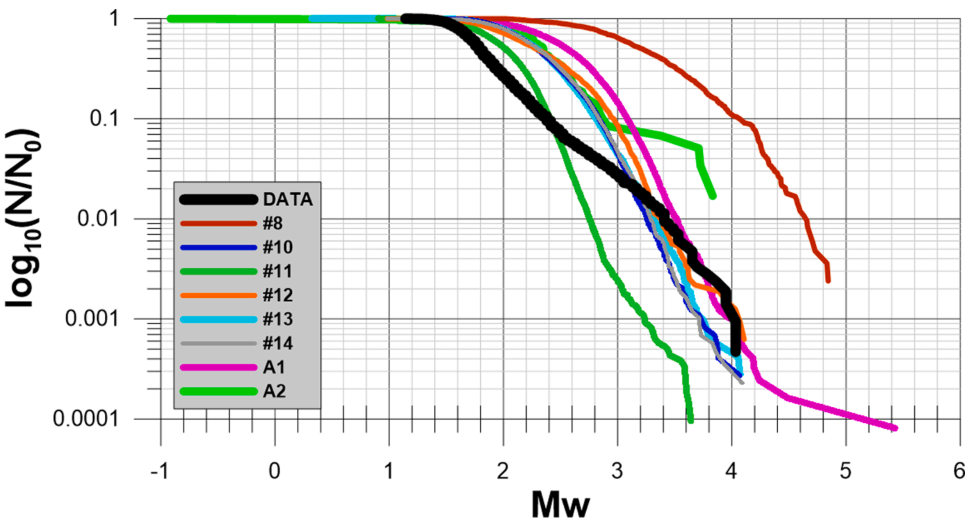

Fig. 7. Gutenberg-Richter seismicity diagram: MEQ's micro-earthquakes data under Mutnovsky volcano 01.2009–10.2020 and MEQ generated on the hydro-mechanical model (CFRAC) of magma injection into the existing fracture with 30° dip angle (static/dynamic option) for modeling options with hydrostatic water gradient in the host rock masses (modeling scenarios ##8, 10–14, Table 3).
Notes: Mw=exp(2.133+0.063×Ms)−6.205, Ms≤5.5; Mw= exp(−0.109+0.229×Ms)+ 2.586, Ms≥5.5; Lolli et al., 2014, p.813, Ms=(Ks-4.6)/1.5, Fedotov, 1972, p.67.

If magma is considered as the fluid phase controlling the effective stress in the host rock massifs, then the trends of effective stresses in the fracture-fracture coordinate system are: $\frac{\partial\sigma_{xx}}{\partial z}$ = –1.0 MPa/km, $\frac{\partial\sigma_{yy}}{\partial z}$ = –1.3 MPa/km, $\frac{\partial\sigma_{zz}}{\partial z}$ = –1.7 MPa/km, $\frac{\partial\sigma_{xz}}{\partial z}$ = –0.6 MPa/km.

2.2.2. *Modeling results*

Seventeen simulation variants were performed at different values of magma viscosity, magma injection flow rate and time, initial magma pressure in the fracture, difference in static and dynamic friction coefficients, size and initial dyke-fracture aperture (Table 3). As a result of modeling, the distributions of the following characteristics in the fracture-dyke were obtained: fluid pressure, normal and shear effective stresses, vectors of shear strains, fracture aperture, hypocenters and magnitudes of microearthquakes (MEQ) for different time moments. The goal of the simulation was to obtain the correspondence between the statistics of the observed and model-generated earthquake swarms on the Gutenberg-Richter diagram (Fig. 7).

The simulation results for the variants (#1–9, Table 3) show that changes in the magma injection flow rate, initial magma pressure in the fracture, shear modulus, and initial fracture opening do not significantly affect the values of the model distribution of earthquake magnitudes Mw, which seemed on average to be one order greater than actually observed.

Results of modeling by variants (#10–14, A1-A3, Table 3) allowed us to discover that when the difference between μdynamic (dynamic friction coefficient of fracture walls) and μstatic (static friction coefficient of fracture walls) decreased to 0.01, the values of model-generated Mw earthquake amplitudes decreased and the values of observed and model-generated earthquakes became consistent (Fig. 7). At the same time, the number of model-generated earthquakes during a single magma injection increased to the first thousand (#10,12–14, Table 3) or to the first tens of thousands (#11, A1, Table 3), although the actually recorded maximum number of MEQ in one cluster is 61. Decreasing the size of the fracture-fault (#A1-A3, Table 3) leads to a significant decrease in the number of earthquakes (up to the first tens) and their magnitudes. Also, some weak MEQ's may missed to register, that's pointed on necessity to increase number of Mutnovsky network of seismic stations.

The results of CFRAC modeling variant #10 (Table 3) are shown in Figs. 8A and 8B. Fracture opening occurs upwards and is characterized by fluid pressure from 98 to 118 MPa, effective normal stress drops to zero in the opening zone, shear deformations during injection generate 7318 microearthquakes with magnitude Mw up to 4.07 distributed throughout the fracture plane (Fig. 8A and Table 3). Opening of the fracture reaches 0.05 m (in the upper part) and 0.0003 m (in the central part) (Fig. 8B). The hanging block of the fracture moves upward relative to the lying block (thrust). In the central part, the shear displacements reach 9 m. The effect of opening the upper part of the fracture-dyke during magma injection, while the lower part of the fracture remains closed (Fig. 8A) obtained from the model. This corresponds to the observed positioning of seismogenic fracture in the NE sector of Mutnovsky volcano with a shift relative to the volcano magma feeder channels against the dip direction in accordance with the values of magma fluid pressure gradients of 14. 0 MPa/km and the effective stress ($\frac{\partial\sigma_{zz}}{\partial z}$ = 21.0 MPa/km) in the coordinate system referenced to the plane of the considered fracture-dykes (see above Fig. 7).

Note also that when the mass flow rate (volume) of magma injection is changed and the values of the other parameters are fixed, the total seismic energy released increases significantly (comparison of variants #3 and #4, #10 and #12). This suggests the possibility of the existence of an empirical relationship between the volume of magma injection and the total seismic energy released.

3. Magmatic gas recharge into production reservoir based on Mutnovsky GeoPP P_{NCG}, blowing wells and thermal features observational data

Magmatic gasses are considered as a component of dykes, injected from Mutnovsky volcano magma system into adjacent production geothermal reservoirs. Mutnovsky GeoPP has two turbines 25 MWe each and two separators, which fed turbines by steam. Wells 24, A2, Geo-3, O29W, O16, GK1 are connected to separator 1, wells O42, O13, O17, O37, Geo-2 are connected to separator-2, see Fig. 2 for wells location. Thus, measuring gas content of total steam production we can monitor magmatic gas additional inflow events, synchronized with magma injections above mentioned. The most reliable and simple method to estimate non-condensable gas content is to measure partial pressure of non-condensable gasses in turbine condenser of the GeoPP.

Aiming estimation of the magmatic gas content, we performed 30-day continuous monitoring of the non-condensable gasses (most of gas content is CO2) partial pressure in the turbine condenser of the

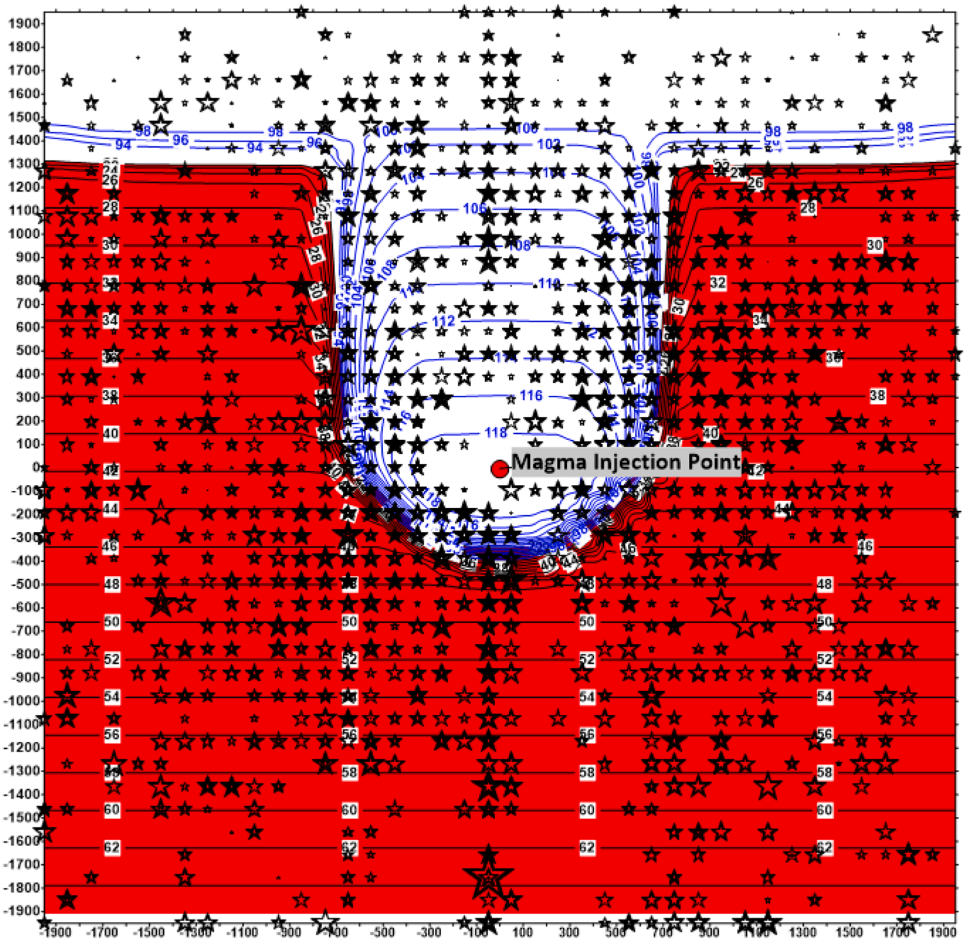

Fig. 8A. CFRAC model results (modeling scenario #10, Table 3) in fracture Y2-Z2 plane (see Fig. 6 for orientation). Distribution of magma pressure in the fracture plane (blue isolines, MPa), effective normal stress (black isolines, MPa), and injection-induced earthquakes (asterisks, size proportional to magnitude) one day after the start of magma injection.

Mutnovsky geothermal power plant during the observational period of time from 25.08.2019 to 25.09.2019. To estimate PCO2 (partial CO$_2$ pressure), we performed simultaneous measurements of the steam condensate pressure Pc and temperature Tc; then, PCO2 was calculated as a difference between Pc and saturation pressure corresponding to temperature Tc.

Fig. 9A shows the transient PCO2 change during the observational period of time from 25.08.2019 to 25.09.2019. It is clearly seen at least 14 maxima of PCO2, which detect non-condensable gas arrivals into the turbine from the production geothermal reservoir. Some of these PCO2 peaks may be related to magmatic gas recharge impulses, followed by or synchronized with the magma fracking processes during dyke #98 injection in production geothermal reservoir described above (see Section 2.1 and Fig. 5A of this paper, note dyke injection time was allowed to be 1 month accordingly to Frac-Digger identification process). Fig. 5A shows 3D view of dyke #98 position in relation to Mutnovsky production reservoirs.

Data from Mutnovsky GeoPP for steam condensate pressure Pc and temperature Tc at the turbine condenser of the Mutnovsky geothermal power plant for 2020 year was also used for P_{NCG} estimations. Fig. 9B matches P_{NCG} transient data with time sequence of dyke injections beneath and adjacent to Mutnovsky volcano detected based on MEQ's data KB FRC UGS RAS (see Section 2.1 of this paper). One can see from Fig. 9B that some dyke injection events follows by P_{NCG} excursions or closely synchronize with them (dykes ##100, 101, 102, 104, 107, 108, 109, 110, 111, 114, 115, 116). Fig. 5C shows 3D view of those dykes positions in relation to Mutnovsky production reservoirs.

Additional source of information on magma injections beneath Mutnovsky volcano are wells blowing on a foot-hills of Mutnovsky volcano (035 and 022, see Fig. 2, Appendix photos 1 and 2). Those wells are located close to epicenter of magma injections zone (Fig. 4). Discreet annual gas-chemical sampling and wellhead temperature measurements (Tables 4A and 4B) shows the following: (1) Water chemistry Na-K geothermometer pointed to temperatures in a range from 254 to 366 °C (well 035) and from 270 to 353 °C (well 022); (2) Wells discharges gas enriched fluids (gas/water ratio from 0.1 to 600 L/kg), mostly of the atmospheric origin. High gas content induces unbearable noise around the wells and also significantly reduce wellhead saturation temperature (like 80 °C at atmospheric pressure in well 035), transparent flow at wellhead is pointed on gas-steam dominated discharge conditions; (3) δ^{13}C ratios pointed to CO2 component of magmatic origin and CH4 component of thermogenic origin; (4) Water isotope corresponds to

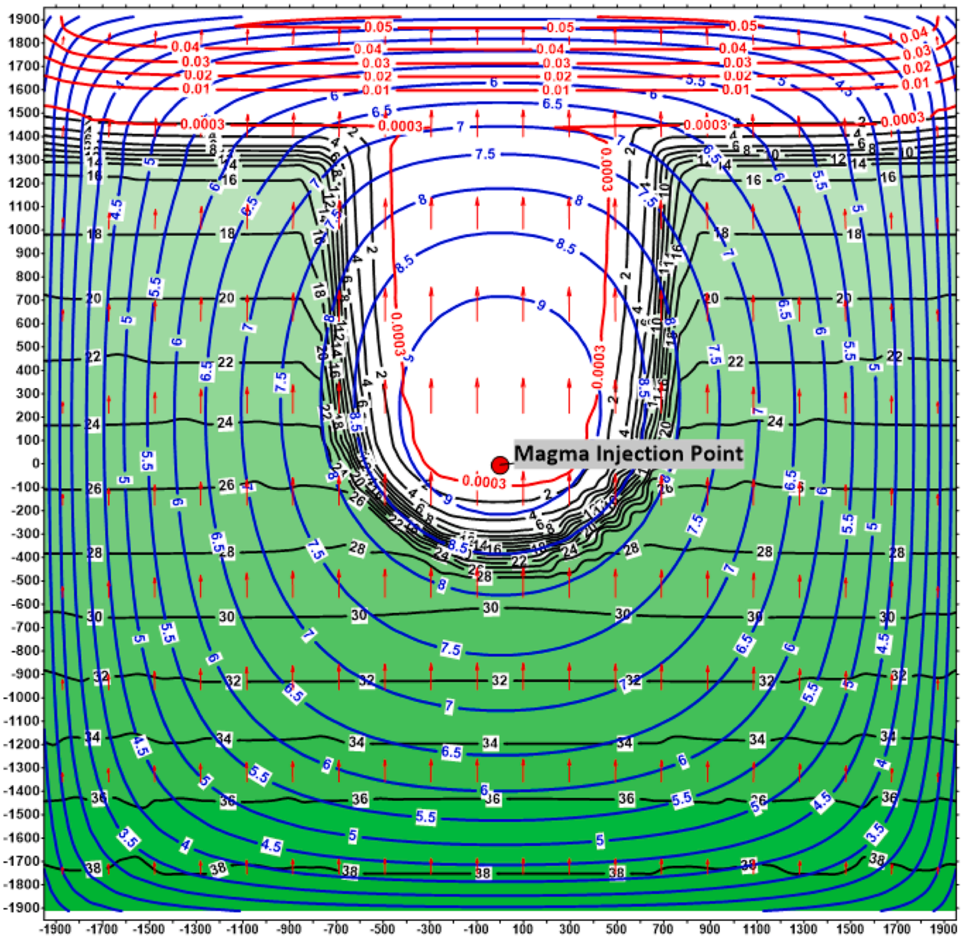

Fig. 8B. CFRAC model results (modeling scenario #10, Table 3) in fracture Y2-Z2 plane (see Fig. 6 for orientation): red isolines - fracture aperture distributions, m; blue isolines - displacements, m; black isolines - shear effective stress, MPa; displacement vectors - hanging block vs. lying block.

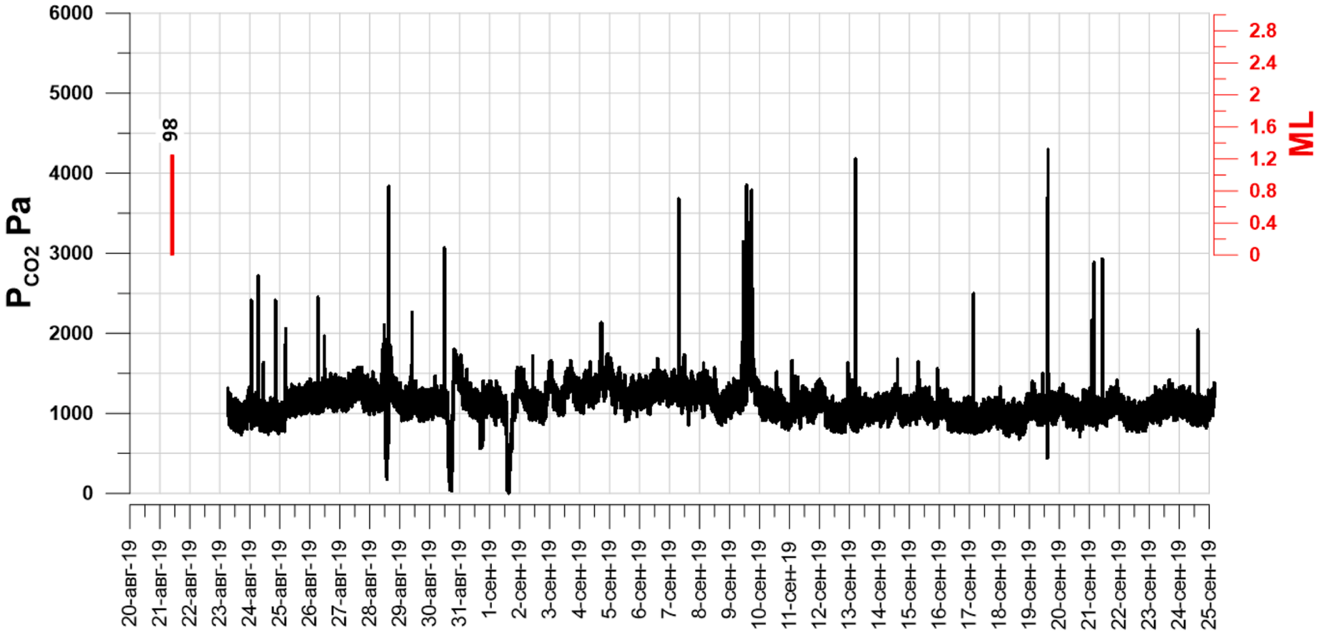

Fig. 9A. P_{NCG} (Pa) in the turbine condenser of the Mutnovsky GeoPP (2019) and dyke injections (ML) in production reservoir vs time. Dykes numbers corresponds to Table 1 and Figs. 4 and 5.

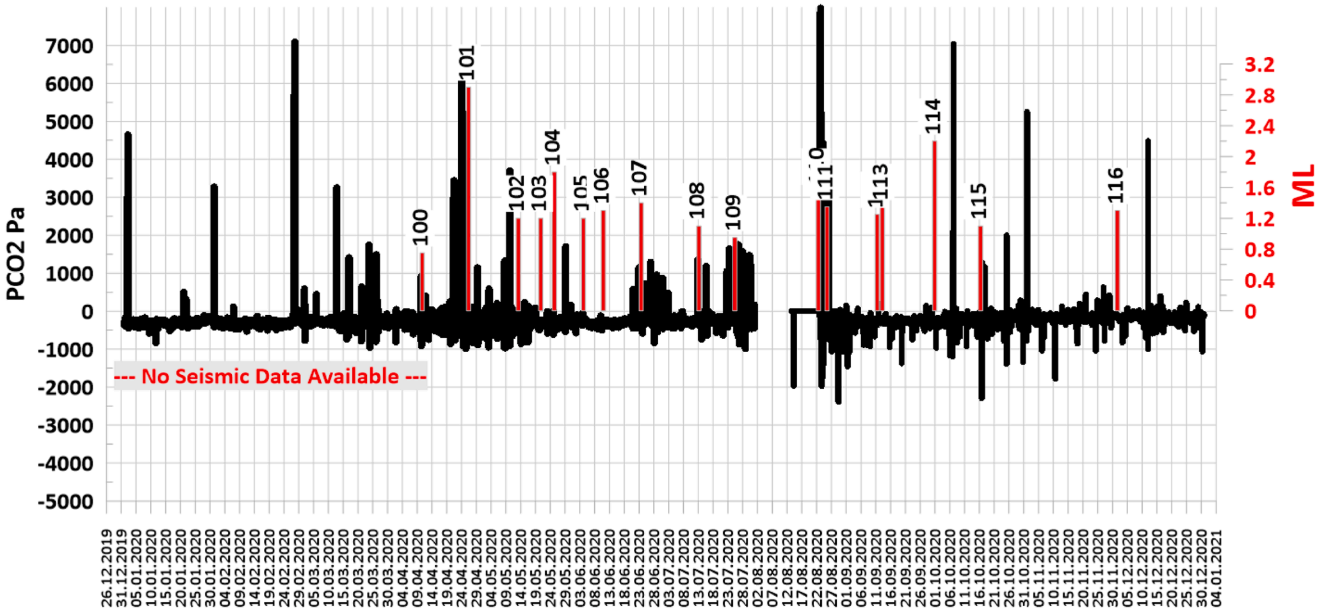

Fig. 9B. P_{NCG} (Pa) in the turbine condenser of the Mutnovsky GeoPP (2020) and dyke injections (ML) in production reservoir vs time. Dykes numbers corresponds to Table 1 and Fig. 4 and 5.

Table 4A

Chemical and water isotope composition of fluids of the Mutnovsky productive wells blowing on a foot-hills of Mutnovsky volcano in 2015–2021. Wells sampled by A. V. Kiryukhin, A.Yu. Polyakov, P.O. Voronin, N.B. Zhuravlev. Chemical analysis performed at the Central Chemical Laboratory of the IVS FEBRAS. Water isotope analysis (samples 2016–2018) performed by P.O. Voronin at LGR IWA 35EP in the IVS FEBRAS, water isotope analysis (samples 2020–2021) performed by I.V. Tokarev in RC RDMI of SPbSU Science Park on Picarro L2120-i laser infrared spectrometer.

Well	Date	pH	HCO_3^-	CO_3^{2-}	SO_4^{2-}	Cl^-	NH_4^+	Na^+	K^+	Ca^{2+}	Mg^{2+}	HBO3	SiO_2	T Na-K	δ_D‰	$\delta^{18}O$‰
O22	17.08.2015	8.9	93	16	96	298	0.0	230	71	1	0.0	152	391	353		
O22	13.09.2016	7.3	37	0	40	70	23.0	48	11	0	0.1	18	389	298	−109.4	−14.9
022	13.08.2017	6.9			37	64	15.0	52	10		< 0.1	28	220	270	−107.2	−15.6
022	09.08.2018	8.6	104		20	4		64	0	5	0.3	2	15		−101.5	−12.8
022	07.08.2019	4.4	< 1.0		274	192	5.3	193	62	2	< 0.1	132	139	359		
022	11.08.2020	6.0	77		91	251	6	173	40	2	< 0.1	119	1075	300		
022	08.08.2021	7.7	57		115	234	6	186	37	1	<0.1	75	156	276	−99.0	−12.0
O35	17.08.2016	5.5	1	0	87	7	13.0	23	6	6	0.8	57	323	321	−103.4	−13.1
035	12.08.2017	4.4			48	21	6.0	33	6		< 0.1	31	187	254	−101.0	−14.6
O35	10.08.2018	7.3	10		52	12	6	24.3	6.6	2	0.7	58	211	328	−104.0	−12.8
035	10.08.2019	4.0	< 1.0		13	52	5.6	25	8	1	< 0.1	180	180	366		
035	15.09.2020	6.9	17		14	5	11.4	7	2	< 0.5	< 0.1	29	67	338	−112.0	−15.2
035	06.08.2021	7.6	8.5		48	7	10	16	3	< 0.5	< 0.1	19	183	267	−103.0	−13.0

Table 4B

Gas composition (vol.%) and carbon isotopic composition of the Mutnovsky productive wells blowing on a foot-hills of Mutnovsky volcano in 2014–2021. Wells sampled by A.V. Kiryukhin, A.Yu. Polyakov, P.O. Voronin, N.B. Zhuravlev. Chemical analysis was carried out at the Central Chemical Laboratory of the Far East Branch of the Russian Academy of Sciences. Isotope analysis (δ13C) was performed by B.G. Pokrovsky (IGEM RAS).

Well ##	Date	T °C	H_2	Ar	O_2	N_2	CO_2	CH_4	$\delta^{13}C$ (CH_4)	$\delta^{13}C$ (CO_2)	R L/kg
O22	13.09.2016	107		1.00	22.10	69.00	4.45	0.00		−7.8	
O22	13.08.2017	121	н.о.		19.94	78.01	1.09	0.01			
O22	09.09.2018	128	0.00	0.10	1.49	96.80	1.69	0.00	−22.1		3
O22	07.08.2019	95	0.01	0.95	15.21	80.29	3.50	0.04			0.1
022	11.08.2020	91	0.28	0.75	18.0	77.8	3.1	0.1		−14.1	8
022	08.08.2021	85	0.1	0.79	18.8	78.6	1.8	0.03			
O35	17.08.2016	>100	0.02	0.80	21.30	73.80	0.64	0.00		−6.9	
O35	**12.08.2017**	**48**	**4.75**		**0.20**	**5.33**	**88.5**	**0.94**			
O35	10.08.2018	98	0.01	0.72	18.76	79.29	1.23	0.01	−19.8		
O35	10.08.2019	80	0.01	0.90	19.57	78.33	1.18	0.01			
O35	11.08.2019	80	0.02	0.91	19.72	78.51	0.84	0.01			600
035	08.08.2020	81	0.04	0.80	18.7	79.7	0.76	0.01		−27.8	
035	14.09.2020	81	0.16	0.83	17.8	79.6	1.5	0.05		−25.0	
035	06.08.2021	80	0.004	0.76	18.7	79.4	1.2	0.003			

Table 5
Gas composition (vol.%) and isotopic composition of carbon in Donnoe Pole (#2, Fig. 2) in crater of the Mutnovsky volcano in 2014–2021. Sampled by A.V. Kiryukhin, A.Yu. Polyakov, P.O. Voronin, N.B. Zhuravlev and A.V. Sergeeva. Chemical analysis was carried out at the Central Chemical Laboratory of the Far East Branch of the Russian Academy of Sciences (V.I. Guseva). Isotope analysis ($\delta^{13}C$) was performed by B.G. Pokrovsky (IGEM RAS).

##	Date	T°C	H_2	Ar	O_2	N_2	CO_2	CH_4	$\delta^{13}C$ (CH_4)	$\delta^{13}C$ (CO_2)	R L/kg
Donnoe Pole	18.08.2014		13.0	0.10	0.70	5.70	55.60	0.04			
Donnoe Pole	19.08.2016	89	6.30	0.14	2.69	15.7	69.49	0.01		−18.3	
Donnoe Pole	18.08.2017	73	1.18		10.7	52.53	35.51	0.00			
Donnoe Pole	11.08.2018	98	0.85	0.04	0.09	2.32	96.68	0.02	−5.9		
Donnoe Pole	11.08.2019	98	1.06	0.03	0.22	3.36	95.33	0.01			20
Donnoe Pole	10.08.2020	90	1.98		0.9	5.4	91.7	0.03		−4.6	20
Donnoe Pole	07.08.2021	95	1.4		0.5	4.6	93.4	0.01			

Table 6
Hydrothermal explosions and landslides in Mutnovsky crater 1996–2021.

Date	Event	Reference/ figure/photos
17.03.2000	Hydrothermal explosion in south part of Mutnovsky crater: acid lake was formed (area of 2500 m2, 3 m deep, temperature of 50 °C, mineralization of 17 g/L)	Gavrilenko et al., 2008 Fig. 2, Appendix, photo 3
May 2003	Acid lake warm-up to 35°C, water convection was observed in the lake.	Gavrilenko et al., 2008
16.04.2007	On April 16, 2007 NOAA-17 satellite detected an ash cloud southeast of the Mutnovsky volcano with area of 22 km x 34 km. The parent explosive crater of 180 *m* × 215 m and about 30 m deep was embedded in the southwest wall of the Active Crater. On the bottom and walls of the Active Crater itself lay debris from the volcano's parent rock, and fresh gray ash was found on the outer slopes of Mutnovsky	Gavrilenko et al., 2008, Appendix, photo 4
03.07.2013	According to F.A. Farberov, an EMERCOM official, on July 3, 2013 at approximately 23:40 UTC, strong fumarolic activity was first observed at the bottom of the Active Crater, and then ash emissions began to occur. Fortunately, the activity of the volcano was moderate, and none of the observers were injured.	Girina et al. 2014
24.03.2018	24.03.2018 Explosive lake was found in Active Crater. Observations on 11.08.2018 (A. Kiryukhin) shows that lake was cold, lake crater area was estimated as 30 m x 50 m and crater lake depth of 10 m.	L. Tavignot, pers. Com, Appendix, photo 4
07.2020	A new small explosion crater diameter of 3 m and depth of 2 m was found 15 m west from "Donnoe Pole" monitoring fumarole point	Sergeeva A. (19.07.2020), Kiryukhin A. (10.08.2020)
06.2021	Active steaming with the rise of a column of steam and boiling puddle on the hiking trail to the Active Crater of Mutnovsky volcano was emerged.	A.Konovalov, pers. com, 2021
18.08.2021 07:32 Local Time	Landslide of the north rim of Mutnovsky-3 volcano crater (approximately 1 mln m^3), Volcannaya river was dammed and lake was created	KB FRC UGS RUS Appendix, Photo 5

meteoric waters at elevation around 1000 m. This may be interpreted as a result of magma-meteoric water interactions, when dykes injected into unsaturated zone above piezometric level of production geothermal reservoir (Fig. 5A). One gas sample of 12.08.2017 in a well 035 seems enriched by magmatic CO_2, that may be timely synchronized with dyke injections in a close vicinity of this well.

Mutnovsky crater is a field of significant phreatic-magmatic activity in a last 20 years (Table 6) after Mutnovsky GeoPP started its large scale operations, although no signs of hydrothermal explosions were seen during 20-years interval before. There were three significant hydrothermal explosions there with volumes of 7 500 m^3 in 2000, 1 160 000 m^3 in 2007, and 15 000 m^3 in 2018 (Table 6, explosions volumes in 2000 and 2007 years were estimated from (Gavrilenko et al., 2008) observational data). Thermal features in Mutnovsky crater are useful to detect magmatic activity too. We do monitoring of the fumarole at the entrance of crater (located in Donnoe Pole) for these purposes. Gas chemistry transient data (Table 5) reveals CO_2 rise during last three years (2018—2020).

In 2021, the magmatic activity of Mutnovsky volcano intensified compared to the preceding 2009–2020. Injections of four dikes and three sills were detected in the area of Mutnovsky volcano during the period from 07.05.2021 to 24.08.2021. Landslide of the north rim of Mutnovsky-3 volcano crater (approximately 1 mln m^3) took place on 18.08.2021 07:32 local time, detected by seismic records of KB FRC UGS RAS and observed two hours later by numerous visitors as a blocks of clastic rocks at the entrance of the Mutnovsky crater. As a result of this disaster Volcannaya river was dammed and damming lake was formed (Appendix, photo 5). The collapse of the northern wall of the crater of Mutnovsky volcano, which occurred on 18.08.2021, is most likely a thermal consequence of magmatic injections above mentioned (which is also a subject of further study).

4. Production faults in Mutnovsky hydrothermal reservoir

Plane-oriented analysis used for production faults identification in the Mutnovsky geothermal reservoir was presented in Kiryukhin et al., 1999, Kiryukhin, 2005, and Kiryukhin et al., 2018. This study applies the program Frac-Digger2 (Russian reg.#2017618050) to extended set of production feed-zone data in order to define production faults parameters (dip angle, dip azimuth, and production fault planar area), by using the top elevations of the production feed-zones as input data.

Input data include: 46 production feed-zones (Asaulov et al., 1987) with add of wells A2(2), A3(2) and A4 data, and data of recently drilled deviated wells Geo-1(4), Geo-2(6), Geo-3(4) and Geo-4(5) (Spektor and Platonova, 2016; Usacheva et al., 2020). The method of plane-oriented clusters parameter estimation in Frac-Digger2 is the same as that in Frac-Digger (see Kiryukhin and Kiryukhin 2016,2017 for details of Frac-Digger), but the difference is in the cluster selection algorithm. The time-ordering sequence of MEQ's is used in Frac-Digger as input, while a stochastic Monte-Carlo approach is used in Frac-Digger2 to select input production feed-zones for subsequent plane-oriented verification.

The following criteria used to define plane-oriented cluster of production feed-zones, forming a production fault: 1. Each production feed-zone may not belong to more than one production fault; 2. The maximum distance between the production feed-zone and approximation plane is $\delta_z = 200$ m; 3. The maximum horizontal distance between production feed-zones in production fault is $\delta_R = 4$ km; 4. Maximum number of production feed-zones included in a production fault.

Table 7A (base reference scenario without deviated Geo-wells 1–4) and Table 7B (extended data set, including deviated Geo-wells 1–4)

Table 7A
Principal production faults, Main (1) and North-Eastern (2) of the Mutnovsky geothermal field are defined as 2D clusters of production feed-zones using Frac-Digger2 program. Note: The total number of production feed-zones used for estimation was 27 (base scenario).

Production faults ##	Dip angle(deg)	Dip azimuth (deg)	X m	Y m	Z m	Number of prod. zones	Area, km^2	Initial production,kg/s
1	53	113	45,586	23,228	−98	19	5.9	371.0
2	43	162	47,111	24,470	−112	6	1.6	261.5

Table 7B
Principal production faults, Main (1) and North-Eastern (2) of the Mutnovsky geothermal field are defined as 2D clusters of production feed-zones using Frac-Digger2 program. Note: The total number of production feed-zones used for estimation was 46 (extended scenario, deviated Geo-wells 1,2,3,4 added).

Production faults ##	Dip angle(deg)	Dip azimuth (deg)	X m	Y m	Z m	Number of prod. zones	Area, km^2	Initial production,kg/s
1	50	118	46,106	23,573	−409	33	4.7	451.0
2	46	157	47,207	24,469	−201	10	2.0	360.5

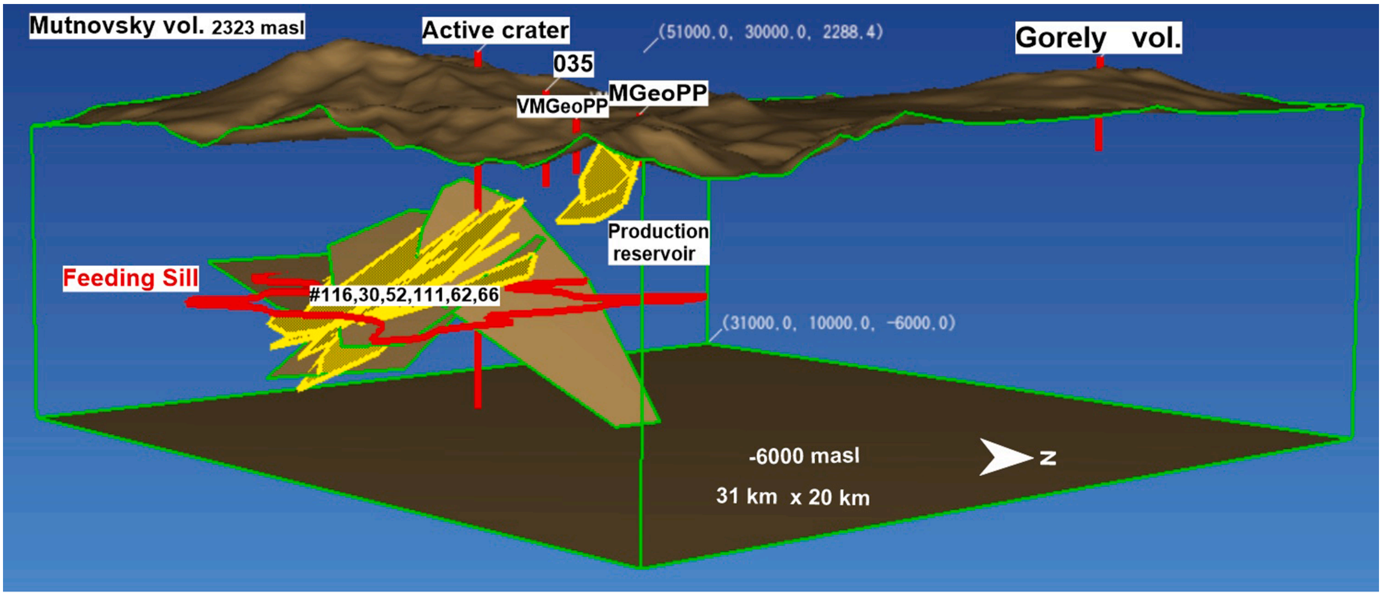

Fig. 10. Production reservoir faults Main (1) and North-Eastern (2) and ten largest (more than 30 MEQ's) clusters (dykes) during time period from 2009 to 2020. Six dykes (116, 30, 52, 111, 62, 66) dip azimuth and strike closely coincide to production faults dip azimuth and strike (Tables 1 and 7).

shows the production faults parameters defined in such a way.

Base scenario shows 25 of 27 production zones nested on a two production faults #1 (Main) and #2 (North-East) (Table 7A), except of wells 049 N and 055 production zones. Production fault plane #1 (Main) includes 19 production feed-zones as follows: wells O16, O29W, A3–1, 8, O45, O1, O14, A2–1, A2–2, O13, 1, A3–2, A4, 26, 4E, O27, O8, O47 and the Dachny thermal feature (#7 in Fig. 2). This nearly coincides with the Main production fault defined by Kiryukhin et al., 1999, 2018. This fault yields 52% of total initial production in the Mutnovsky geothermal field (Table 7A). Production fault plane #2 (Table 7A) includes 6 production feed zones as follows: wells O42, O48, O53N, 24, O37 and the V-Mutnovsky thermal feature (#11 in Fig. 2). This is close to the orientation of the NE production fault delineated in Kiryukhin et al., 1999, 2018. This fault yields 37% of total initial production in the Mutnovsky geothermal field (Table 7B).

Extended scenario (including data of deviated Geo-wells 1–4) also shows most production zones nested on a two production faults #1 (Main) and #2 (North-East) (Table 7B). Production fault plane #1 (Table 7B) includes 33 production feed-zones as follows: O14, A2–1, A2–2, O16, O13, O29W, 1, A3–1, A3–2, A4, 26, 4-E, 8, O8, Geo-1D, Geo-2A, Geo-2B, Geo-2C, Geo-2D, Geo-2E, Geo-2F, Geo-3A, Geo-3B, Geo-3C, Geo-3D, Geo-4A, Geo-4D, Geo-4E 045, 01, 047, Geo-4B, Geo-4C. This nearly coincides with the Main production fault defined by Kiryukhin et al., 1999, 2018. This fault yields 53% of total initial production in the Mutnovsky geothermal field (Table 7B). Production fault plane #2 (Table 7B) includes 10 production feed zones as follows: wells O37, O53N, Geo-1C, 24, O42, O48, O55, Geo-1A, Geo-1B and the V-Mutnovsky thermal feature (#11 in Fig. 2). This is close to the orientation of the NE production fault delineated in Kiryukhin et al., 1999, 2018. This fault yields 42% of total initial production in the Mutnovsky geothermal field (Table 7B).

Thus, 43 of 46 production feed-zones were nested on two production faults, which pointed on a discreet fracture network entity of Mutnovsky production geothermal reservoir, while two production zones of wells O27, O49N were not fitted to production faults above mentioned. Production faults orientation (dip azimuth from 113 to 157°, dip angle from 46 to 50°) closely coincide with the orientation of magma fracking system (Figs. 3 and 10), which pointed on possible involvement of magma fracking processes in formation of production faults in Mutnovsky geothermal field. 3D views of production faults are presented in Figs. 5A, 5B, 5C and 10.

5. Discussion

5.1. *Magma fracking systems as potential production geothermal reservoirs*

Its commonly assumed, that super-critical (SC, with temperatures above 375 °C) or super-hot (SH) production geothermal reservoirs may be found beneath conventional production geothermal reservoirs or may be created there artificially (hydro-thermally fractured) as enhanced geothermal systems (EGS), that may significantly increase efficiency (x10) and capacity of geothermal resources exploitation.

Krafla Magma Testbed (KMT) concept (#1) suggest convection magma systems (in a form of plexus of dykes and sills) as SC geothermal reservoirs (Eichelberger et al., 2020b), and thin lead layer between magma and conventional production reservoir considering as a target volume for SC geothermal reservoirs exploitation (that is indeed heat mining from lead layer using cooling/thermally induced fracking).

Proof-of-concept #1 borehole was IDDP-1, that's 2.1 km deep, drilled in 2008–2009. IDDP-1 penetrated a magma body with temperatures > 900 °C in the Krafla caldera (Iceland) (Friðleifsson et al., 2015). After intense cooling with formation of a permeable zone due to creation of thermally induced fracturing in the crystallized magma, a flow tests were performed (2 years, March 2010 - July 2012). This tests show the possibility to operate the IDDP-1 well with the flow rate of 40–50 kg/s at the wellhead pressure of 40–80 bar (superheated steam). This corresponds to 25–35 MWe production, but for stable operation the problem

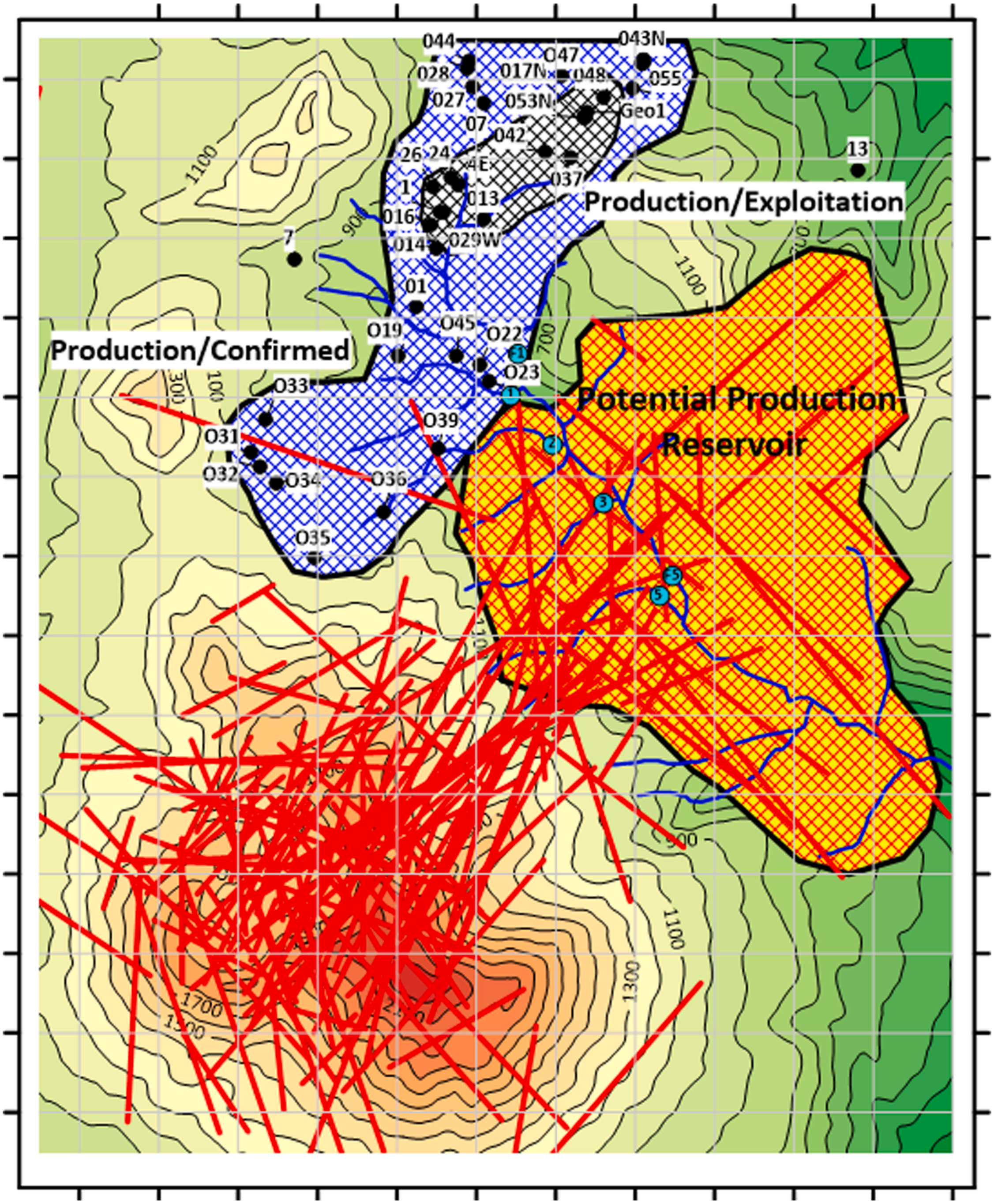

Fig. 11. Potential production geothermal reservoir outside of existing drilling area - a new target for geothermal drilling in Mutnovsky geothermal field. Legend: dykes traces at elevations of −3000 and −1500 m are shown by red lines, potential production reservoir is red cross-hatched area, currently exploited production reservoir is black cross-hatched area, confirmed by drilling production reservoir is blue cross-hatched area, wells are shown by black filled circles with numbers, Falshivaya river is shown by blue lines. Preliminary hydrochemical survey sampling points of Falshivaya river basin are shown by blue circles with numbers, corresponding to Table 8. Axes scale – 1 km, map coverage is the same as Fig. 2.

of steam cleaning from SiO_2 (62 ppm), HCl (100 ppm) and S needs to be resolved (Friðleifsson et al., 2015).

Japanese Beyond Boundary Ductile (BBD) concept (#2) propose granite-batholite systems at SC conditions as self-sufficient mid-permeability reservoirs, disconnected from shallow conventional production reservoirs due to silica precipitation barrier (Tsuchiya, 2020), and SC batholites are considering as a target volume for SC geothermal reservoirs exploitation.

First proof-of-concept #2 borehole was WD-1a in Kakkonda (Muraoka et al., 1998). This well deeply penetrated into granite at SC conditions, but show zero permeability there. The next one was IDDP-2 in Iceland, which met SC conditions at 4.5 km depth (Halldursdottir et al., 2020). It was attempted to convert bottom feedzone in CDM (convective downward migration) mode using cold water injection and injectivity index of 3.1 kg/s/bar was achieved (Sigurdsson, 2020). Its anticipated to get several hundreds of GWe from such SC geothermal reservoirs in NE of Japan (Asanuma et al., 2020).

In this paper we suggest to use active magma fracking volumes (natural EGS), or magma injections space in a form of dykes/sills swarms identified by MEQ’s distributions (Figs. 4 and 5), as a target volume, where potential production geothermal reservoirs are resides. In this case no need to artificially convert them into EGS using hydro-fracking, which active volcano already done. Moreover, magma quick solidification within thin dykes and sills may drastically enhance its permeability by ten orders of magnitude, following cooling induced contraction fracturing mechanisms (Lavallée et al., 2020). Heat supply in this system is permanently coming with magma injections and fluid upflow, if recharging roots are deep enough.

Accessible by drilling (topo surface elevations below 1200 m) magma fracking volume in the northeast sector of the Mutnovsky volcano is defined in area of 30.3 km^2 as shown in a Fig. 11 and Appendix, photo 6. The range of depth where magma fracking took place is estimated from −4 to −2 km (Fig. 3), reservoir temperature is estimated to be from 254 to 366 °C, accordingly to Na-K geothermometer indications of adjacent wells 022 and 035 (Table 4A). That is significantly exceed the currently exploited Mutnovsky geothermal field area of 2.9 km^2 (62 MWe installed, 45 MWe actual output), where production operation temperatures in a range from 240 to 270 °C.

5.2. Magma fracking, frequency of hydrothermal eruptions in Mutnovsky crater and adjacent strong EQ’s

Another important issue is a relationship between magma fracking beneath and adjacent to active Mutnovsky volcano, hydrothermal explosions in Mutnovsky volcano crater and strong earthquakes caused by Pacific plate subducting (simultaneously recharging volcanic activity).

Worth noting tourist attraction of the Mutnovsky volcano crater, where in a summer time period from June to September a number of visitors may reach up to 300 persons per day, in spite of danger of phreato-magmatic explosions (see Section 3, Table 6). There are worldwide examples of such eruptions following human casualties and death (Eichelberger et al., 2020a). In Japan, the eruption of Mount Ontake on 27 September 2014 killed 63 climbers (noting, this eruption was preceded by a ten-year period of gas influx (CO2) under the volcano). The most recent magma–hydrothermal event was the explosion at a popular tourist destination, Wakaari/White Island Volcano, New Zealand on 9 December 2019. Forty-seven tourists and their guides were in the crater at the time of the eruption, of whom 21 died and 26 were injured, most of the latter seriously.

Strong earthquakes is another threat. According to the long-term seismic forecast (Fedotov et al., 2019) one of the two most dangerous seismic gaps in the entire Kurilo-Kamchatka seismogenic zone is located in the coastal zone adjacent to the area of the Mutnovsky GeoPP. Five-year probability of the strongest ($M \geq 7.7$) earthquake in this area with expected destructive 8-ball shaking in Petropavlovsk-Kamchatsky is about 20%, which is several times higher than the long term average.

Fig. 12 integrates magma fracking events (dykes) beneath and adjacent to Mutnovsky volcano with strong earthquakes (Ks>13.5, ML>6.0, on a distance of less than 125 km) and phreatomagmatic explosions in Mutnovsky volcano crater during time period from 2000 to 2021 (note magma fracking detection was possible after 2009 only, since no seismic network was available here before). Here we see crater

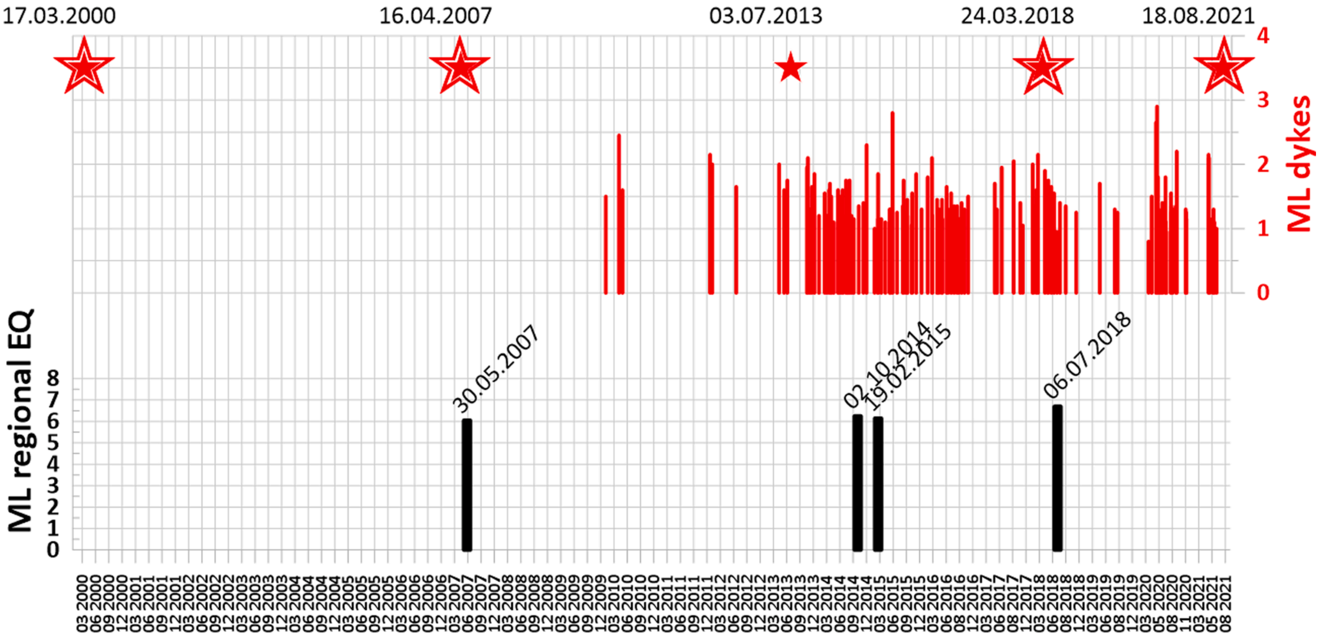

Fig. 12. Mutnovsky volcano magma fracking activity (dykes, shown by corresponding ML bars), crater eruptions and landslide of 18.08.2021 (stars, corresponding to Table 6, with double stars most significant) and adjacent strong regional earthquakes (ML>6.0, located on a distance of less than 125 km, see Fig. 1). Note: no magma fracking events were detected before 2009 because of absence of local seismic network. Lock of seismicity data is also sometimes occurs in a winter periods due to seismic network operation fails.

Table 8
Chemical and water isotope composition of water of the Falshivaya river basin in northeast sector of Mutnovsky volcano. Sampling was performed by A.V. Kiryukhin. Chemical analysis performed at the Central Chemical Laboratory of the IVS FEBRAS. Water isotope analysis was performed by I.V. Tokarev in RC RDMI of SPbSU Science Park on Picarro L2120-i laser infrared spectrometer. Sampling points locations are shown in Fig. 11.

##	Date	pH	HCO_3^-	SO_4^{2-}	Cl^-	Na^+	K^+	Ca^{2+}	Mg^{2+}	H_3BO_3	SiO_2	$T_{Na\text{-}K}$	δ_D‰	$\delta^{18}O$‰
F1	08.08.2021	6.2	13	87	36	40	7	4	1	14	156	257	−98	−13.4
1	08.08.2021	6.8	1	19	4	2	<1	6	1	3	20		−100	−14.2
2	08.08.2021	4.7	<1	115	<1	5	<1	30	4	<0.5	27		−103	−14.6
3	08.08.2021	7.2	1	11	1	4	<1	3	1	<0.5	23		−101	−14.1
5	19.09.2021	4.5	0.1	250	3	8	1	77	9		14	213	−102	−14.4
5	19.09.2021	5.0	0.2	220	4	9	1	80	9		11	199	−102	−14.4
F5	19.09.2021	7.2	18	56	17	28	4	10	2		22	229	−97	−13.5

pre-explosion sequence of dykes, which lasted during 5 years before explosion of 24.03.2018. Since 04.2020 a new generation of pre-explosion dykes was grown, which ended by Mutnovsky crater landslide of 18.08.2021 (Appendix, Photo 5). Four strong earthquakes ($M>6$) located in 125 km vicinity of Mutnovsky volcano were preceded by Mutnovsky crater hydrothermal explosions in 2007, 2013 and 2018 are in a range of times from 1.5 months to 1.3 year in advance. A possible mechanism of such pre-cursor events may be activation of fluid generation in subducting plate, which may cause volcanic magma recharge increase and time delayed regional seismogenic faults slip.

6. Conclusions

6.1 Magma fracking beneath Mutnovsky volcano detected by MEQ's observational data pointed on shear mode low angle dykes in northeast sector and opening mode geomechanical conditions in a range of depth from −4000 to −2000 m, where sills in area of 62 km^2 are suggested to be formed preferably at a depth of −3000 m. Mutnovsky volcano low angle dykes injections were reproduced by hydromechanical simulation using CFRAC, modeling results matches with MEQ's statistics observed.

6.2 Magma injections associates with NCG (CO_2) release in production reservoirs, which is detected by partial NCG pressure excursions at GeoPP condenser. Mutnovsky GeoPP steam collection system shows sensitivity to NCG content (partial gas pressure) variations (2019—2020), that is used as an indicator of magmatic gasses recharge via volcano magma fracking to production geothermal reservoir. Partial gas pressure can easily measure at GeoPP condenser unit. Some signs of magma fracking events were also revealed using discreet observations (2016–2021) on a blowing wells on a foot hills of Mutnovsky volcano.

6.3 A new potentially production geothermal reservoir was identified adjacent to northeast foothills of Mutnovsky volcano (depth range from −4000 to −2000 m, accessible area of 30 km^2) based on MEQ's data analysis. MEQ's focal mechanism information may be useful for proposed reservoir verification, to implement this, additional seismic stations deployment in a vicinity of Mutnovsky volcano is required. This reservoir should be verified by others geophysical and geochemical methods (including chloride tracer method (Kiryukhin et al., 2022) and subsequent exploration drilling. Preliminary hydrochemical survey of Falshivaya river basin adjacent to northeast sector of Mutnovsky volcano (Table 8) reveals anomalous sulfate ion discharge and high values of $T_{Na\text{-}K}$ geothermometer in one of tributaries, coinciding to dykes injections area (Fig. 2).

6.4 Magma fracking beneath Mutnovsky volcano associates with small and medium hydrothermal explosions and landslides (2009–2021). Thus, magma fracking dynamics analysis (including monitoring of the partial NCG pressure excursions at GeoPP) may serve as a warning tool for tourists trips planning in Mutnovsky volcano crater. A correlation between magma fracking activity and strong earthquakes must be analyzed too.

Author's contributions

All authors have read and agreed to the published version of the manuscript.

Funding

This study was funded by RFBR and JSPS according to research project # 21-55-50003.

CRediT authorship contribution statement

A.V. Kiryukhin: Conceptualization, Methodology, Software, Validation, Data curation, Visualization, Writing – original draft, Writing – review & editing. **A.Y. Polyakov:** Data curation, Formal analysis. **P.O. Voronin:** Field works. **N.B. Zhuravlev:** Field works. **O.O. Usacheva:** Data curation, Visualization. **A.V. Solomatin:** Formal analysis. **P.A. Kiryukhin:** Software.

Declaration of Competing Interest

The authors declare no conflict of interest. The funders had no role in the design of the study; in the collection, analyses, or interpretation of data; in the writing of the manuscript, or in the decision to publish the results.

Acknowledgement

Authors express gratitude to M. McClure and R. Horne for CFRAC permission to use, V.Lavrushin for gas C-13 isotope analysis accommodation, A. Lyubin and M. Bezotechestva for sharing MGeoPP condenser P-T data, N. Tsuchya for sharing knowledge of Japanese SC BBD data. Authors appreciated three unknown reviewer's for comments and suggestions, which help a lot to improve manuscript of this paper.

Appendix (Photos)

Photo-1 Blowing well 035 at the foothills of Mutnovsky volcano (see Fig. 2 for well location). Photo by A. Kiryukhin, 2005. Unbearable noise around this well and significant reduce of wellhead saturation temperature (down to 80 °C at atmospheric pressure) was observed here since 2017.

Photo-2 Blowing well 022 at the southeast of the existing production Mutnovsky reservoir (see Fig. 2 for well location), white silica deposition covers on the background. Photo by A. Kiryukhin, 2020. Unbearable noise around this well and significant reduce of wellhead saturation temperature (down to 91 °C at atmospheric pressure) was observed here since 2019.

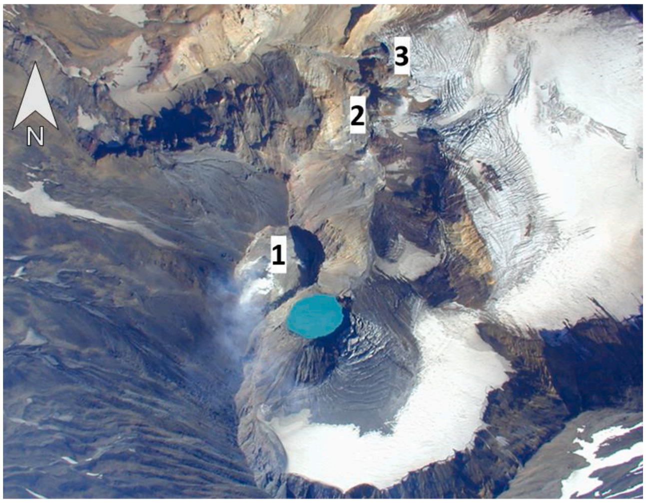

Photo-3 Mutnovsky volcano craters aero-view. Explosion crater of 2000 is a blue acid lake, thermal features: 1- Active crater, 2 – Bottom Field, 3- Upper Field (see also map in Fig. 2). Background photo by N. Seliverstov, 2000.

Photo-4 Mutnovsky volcano Active crater with recent explosion craters inside: 1 – explosion crater 2007, 2 – explosion crater 2018 with a water level on a bottom. Background photos by A. Kiryukhin, 2008 (upper photo), 2019 (lower photo).

Photo-5 The collapse and damming lake in the northern part of the Mutnovsky volcano crater (photo by A. Konovalov 19.08.2021).

Photo-6 Mutnovsky volcano, existing production geothermal field and MGeoPP, potential production area. Background photo by A. Kiryukhin, 2008.

Appendix A. Stresses estimations

Calculations to identify Sv, SHmax and Pp are presented below.

Anderson's tectonic stress theory (outlined in Zoback, 2010) assumes that in the rock space it is possible to orient a cube along the directions of principal stresses (on the faces of the cube the pressure forces normal), and one of the axes of the cube is vertical. In this case the stresses are defined as pressures on planes of given orientation. Accordingly, we assume the following notation: Sv - vertical stress, SHmax - maximal horizontal stress, Shmin - minimal horizontal stress. Here we determine the geomechanical state of the rock massif NF (Normal Faults, horizontal tensile stress) - to conditions Sv > SHmax > Sh min; SS (Strike Slip, horizontal shear) - corresponds to a condition of SH max > Sv > Sh min; RF (Reverse Faults (thrusts) - fits the condition SHmax > Sh min > Sv.

Let us define the vertical stress Sv (rock or lithostatic pressure) as the pressure of the overlying fluid-saturated rocks:

$$S_v = \int_0^z \left(\rho_R(1-\varnothing) + \rho_f\varnothing\right) \text{g dz} \tag{A1}$$

where ρ_R is the mineral density of rocks, ρ_f - fluid density, ϕ - porosity.

Pore pressure Pp, or fluid pressure, is defined as the pressure of the fluid at a given point in the pore-crack space of the rock massif. In this study we assume Pp is equal to hydrostatic pressure, that is defined as the pressure of the water column from the piezometric water level to the considered point of the rock space.

Fig. A1 shows the corresponding dependence of changes in vertical stress Sv and pore pressure Pr on depth for conditions in the Mutnovsky volcano area, with characteristic petrophysical properties and lithology along the section given in Table A1.

The theory of frictional equilibrium (Zoback, 2010) suggests that active crustal fractures are in an extremely close to sliding state, i.e. the Mohr's circle touches the Coulomb line of destruction. This makes it possible to obtain equations of frictional equilibrium for various geomechanical states (NF, SS, RF) and perform estimations of extreme (minimum and maximum) effective stresses (S-Pp). As applied to the Reverse Faults geomechanical state (RF) equation of frictional equilibrium can be written in the following form:

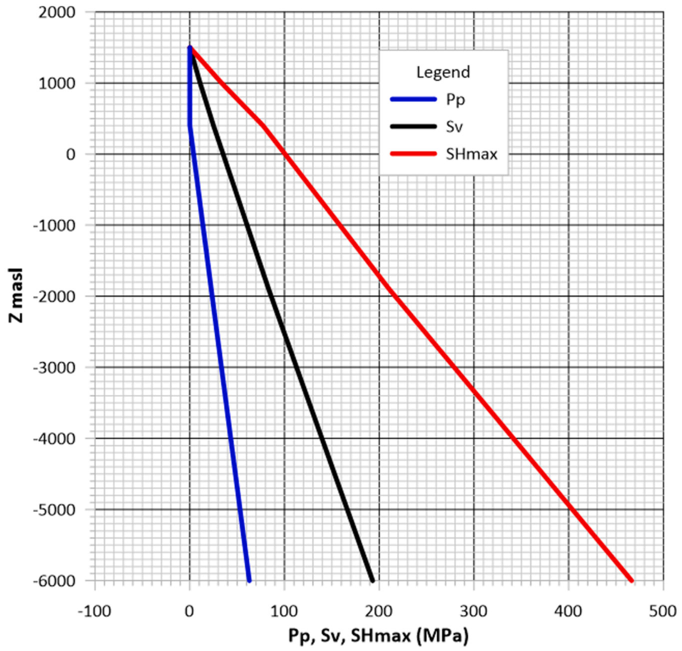

Fig. A1. Dependence of pore pressure Pp, vertical stress Sv, horizontal stress SHmax on depth for conditions around Mutnovsky volcano and Mutnovsky geothermal field (Table A1).

Table A1
Petrophysical properties and saturation of the pore-fracture space of rocks in the Mutnovsky geothermal field area.

Depth range, m	Density of dry rocks, kg/m^3	Porosity	Gas saturationSG	Lithology
1000, 1500	2200	0.30	1	Andesite and basalt lavas $Q_{3\text{–}4}$
400, 1000	2400	0.20	1	Pliocene-Quaternary lavas and tuffs N_2-Q_1
200, 400	2400	0.20	0	Miocene rhyolite tuffs N_1al
−1900, 200	2500	0.08	0	Miocene sandstones Pg_3-N_1
−3500, −1900	2700	0.03	0	Intrusive dyke complex $Q_{3\text{–}4}$

$$\frac{\mathrm{SHmax} - \mathrm{P_p}}{\mathrm{S_V} - \mathrm{P_p}} = \left(\sqrt{(1+\mu^2)} + \mu\right)^2 \tag{A2}$$

At friction coefficient μ=0.6 (Zoback, 2010) the expression $\left(\sqrt{(1+\mu^2)} + \mu\right)^2 = 3.1$

Eq. (A2) allows us to calculate SHmax - based on Sv and Pp data for RF geomechanical conditions, the results of the calculations are shown in Fig. A1.

Appendix B. Frac-Digger and Frac-Digger2, methods of plane-oriented clusters identification

In this study, we assume that the emplacement of magma in a fractured medium beneath active volcanoes is analogous to the injection of fluids into wells with subsequent hydraulic fracturing occurring in their host formations.

Cluster identification was carried out using our Frac-Digger program (RU #Reg. 2016616880). The following is a brief explanation of the algorithm used in this program. The first element of the cluster is removed from the initial list during each iteration. The following criteria are used to include a new event in a cluster: (1) a time difference (δ_t); (2) a distance difference in the horizontal plane (δ_R); and (3) a requirement of a nearly planar orientation (i.e., a distance from the event to the plane (δ_Z). When the resulting cluster contains more than N elements, that cluster is treated as completed and is added to the list of plane-oriented clusters. All elements of a resulting cluster are removed from the initial list of elements (in cases when the cluster size > N). This procedure is then reiterated until the initial list of elements is exhausted.

The calculation of the parameters of a plane-oriented cluster is based on a list of cluster elements. Each element i contains the coordinates (x_i, y_i, z_i). For N (the number of elements in the cluster) points with coordinates (x_i, y_i, z_i), we can find the equation of the fitting plane $z = ax + by + c$ using the least-squares method. The solution thus reduces to solving a set of linear equations as follows:

$$\begin{bmatrix} \sum x_i^2 & \sum x_i y_i & \sum x_i \\ \sum x_i y_i & \sum y_i^2 & \sum y_i \\ \sum x_i & \sum y_i & n \end{bmatrix} \begin{bmatrix} a \\ b \\ c \end{bmatrix} = \begin{bmatrix} \sum x_i y_i \\ \sum y_i z_i \\ \sum z_i \end{bmatrix} \tag{B1}$$

These equations are then solved using Cramer's rule. In this way, we obtain the coefficients a, b, c for the equation of a plane, which is defined as $z = ax + by + c$. The next step is to find the unit vector that is normal to the fitting plane $\boldsymbol{n} = (a/\Delta, b/\Delta, -1/\Delta)$, where Δ is the determinant of the equations that result in the following geological parameters: dip angle $\beta = \arccos(1/\Delta) * 180/\pi$ and the azimuth of dip $\alpha = \arctan(a/b) * 180/\pi$. The analysis of the sensitivity of this algorithm, where plane-oriented clusters are selected according to the criteria of temporal and spatial proximity, indicates that the above criteria produce selection results that are both physically and geologically reasonable (Kiryukhin et al., 2017, Appendix 2).

The Frac-Digger2 program (Russian reg.#2017618050) complements the Frac-Digger program by analyzing almost all possible variants of constructing productive (or seismogenic) faults and horizons over a set of productive zones (earthquake hypocenters). In the program Frac-Digger2, sampling K from a set of points in the 3D-spatial domain is done randomly (Monte-Carlo method is used). This makes it possible to avoid dependence of the solution on the ordering of the initial set of points by time, which is extremely important in 3D analysis of the distribution of productive zones and identification of productive faults. The same method and the same parameters (δ_z and δ_R) as in Frac-Digger are used to check the plane orientation of N-point cluster and to calculate the parameters of approximating plane. If the check is successful, the unused points of the original set that satisfy the criteria of plane cluster orientation are added to the cluster. The criteria for ending cluster selection are: (1) the maximum number of points included in it; (2) the maximum sum of point attribute parameters (which can be earthquake magnitudes, productive zone rates, and other parameters depending on the problem); and (3) the time defined in the program to perform the plane-oriented point cluster selection procedure.

When searching for K elements from a list consisting of N elements, the maximum number of unique C_N^K generations is limited by the iteration time, so several program runs are performed to confirm the validity of the identified productive (seismogenic) faults.

Appendix C. Most reliable Mutnovsky MEQ's set plane-orientation testing

Most reliable Mutnovsky MEQ's sets were published in annual reports of (Zemletryaseniya Rossii v 2009 g. (Earthquakes in Russia in the year 2009), Obninsk: GS RAN, 2009… Zemletryaseniya Rossii v 2019 g. (Earthquakes in Russia in the year 2019), Obninsk: GS RAN, 2019). The total number of available reports is 11, the total number of micro-earthquakes reported in area shown in Fig. 2 is 146. The most reliable sixty-three MEQ's with epicenter error and depth error determination less than 3 km were selected for testing (Table C1).

Table C1
The most reliable MEQ's with epicenter error and depth error determination less than 3 km (data from "Earthquakes in Russia in the year 2009, Obninsk: GS RAN, 2009… Earthquakes in Russia in the year 2019, Obninsk: GS RAN, 2019″).

Data and time	Latitude	Longitude	Epicenter Error	Depth,km	Depth Error,km	Ks
06.04.09 8:49	52.53	158.176	3	1.6	2	5.1
23.01.10 16:11	52.475	158.219	1.2	3.5	0.5	4.1
09.05.10 9:50	52.53	158.202	2.5	4.6	1.3	5.1
15.05.10 17:43	52.522	158.189	1.8	3.9	1.9	4.7
09.06.10 11:25	52.451	158.203	1.5	2.4	0.9	5.4
29.08.10 22:50	52.452	158.238	1.6	−1.5	1	4.5
20.10.10 4:45	52.545	158.135	0.2	−0.9	0.1	4.4
31.08.11 0:12	52.467	158.226	1.4	3.6	0.7	5
10.07.12 4:55	52.532	158.167	1.3	3.7	1	5.3
31.07.12 4:02	52.53	158.222	3	3.9	1.5	6
22.08.12 15:34	52.463	158.295	2	0.1	0.5	5
23.12.12 11:34	52.533	158.19	2.6	6	2	5.2
28.02.14 21:18	52.456	158.182	1	3.8	0.5	4.1
08.03.14 12:26	52.458	158.217	2.1	3.8	0.9	4.5
08.03.14 12:26	52.49	158.181	0.3	1.7	0.1	4.6
11.03.14 1:39	52.468	158.165	2.8	3.1	1.7	4.5
23.06.14 0:29	52.447	158.22	2.4	4.2	1.8	4.7
10.08.14 14:29	52.55	158.26	2.2	6.1	2.3	4.4
06.09.14 12:00	52.518	158.177	1.4	5.1	1.6	4.6
21.10.14 15:52	52.463	158.197	0.6	5.9	1.6	4.2
19.11.14 13:41	52.462	158.207	2.7	3.2	1.6	4.3
15.12.14 11:52	52.459	158.164	2.1	2.2	1.5	4.7
14.05.15 19:08	52.539	158.234	2.7	5.9	1.6	4.1
07.07.15 2:22	52.528	158.198	3	5.8	1.3	4.6
07.07.15 14:31	52.439	158.176	2.6	3.6	1.5	4.1
18.08.15 15:42	52.505	158.195	3	4.4	2.2	4.2
23.09.15 4:43	52.532	158.187	1.8	4.6	0.9	4.2
08.11.15 8:47	52.461	158.201	1.1	3.4	0.4	4.5
09.11.15 10:26	52.494	158.253	2.4	2.5	1.6	4.6
30.11.15 19:32	52.432	158.221	1.8	6	1.4	4.1
08.02.16 0:21	52.443	158.188	2	3.5	2	4.1
17.04.16 3:03	52.463	158.156	2.3	2.9	1.4	4.4
02.05.16 22:57	52.462	158.25	2.9	4.6	1	4.1
09.06.16 6:44	52.467	158.216	1.2	4.5	0.7	4.3
22.06.16 8:47	52.445	158.195	2.5	4.1	2.7	4.8
11.07.16 3:52	52.448	158.197	2.6	3.8	1.7	4.6
17.08.16 15:45	52.492	158.222	2.8	3.4	0.6	4.2
01.09.16 6:48	52.465	158.201	0.6	3.5	0.3	4.2
26.09.16 8:45	52.537	158.192	2.2	4.5	1.2	4.1
13.10.16 17:43	52.492	158.214	3	3.3	0.6	4.1
15.10.16 5:31	52.46	158.202	0.3	3.6	0.1	4.1
15.10.16 13:40	52.459	158.266	1.3	3.8	0.6	4.1
16.10.16 13:38	52.531	158.199	2.2	5.9	1.8	4.2
07.11.16 13:44	52.456	158.195	0.8	3	0.4	4.5
10.03.17 20:20	52.441	158.184	3	4	1.7	5.4
10.09.17 7:30	52.542	158.188	1.7	4.5	1.4	4.6
21.01.18 2:48	52.469	158.218	0.3	3.5	0.1	5.1
21.01.18 20:01	52.464	158.205	0.8	3.9	0.4	5

(*continued on next page*)

Table C1 (*continued*)

22.01.18 13:58	52.461	158.202	0.4	3	0.2	4.9
23.01.18 8:46	52.451	158.198	1.7	3.5	1.3	5
24.01.18 13:40	52.458	158.196	1.2	2.6	0.5	5.2
10.02.18 3:39	52.436	158.217	1.9	0.1	1.3	4.7
21.02.18 7:33	52.442	158.21	2.8	3.6	1.8	4.6
21.02.18 9:35	52.466	158.215	0.9	3.1	0.4	4.7
08.03.18 21:20	52.541	158.199	1.7	4.8	1.5	4.8
08.05.18 21:35	52.461	158.221	1.4	4.7	0.5	5.3
10.06.18 23:59	52.46	158.167	1.8	2.2	0.8	4.8
11.06.18 15:30	52.451	158.144	2.2	−0.1	1	4.6
19.07.18 8:23	52.53	158.139	3	4.7	1.5	5.3
12.01.19 16:00	52.544	158.175	2.4	5.3	1.7	5
18.04.19 9:49	52.457	158.198	2.8	−1.4	1.2	4.9
26.12.19 21:30	52.47	158.164	1.8	1.7	1.5	4.6
26.12.19 21:30	52.47	158.164	1.8	1.7	1.5	4.6

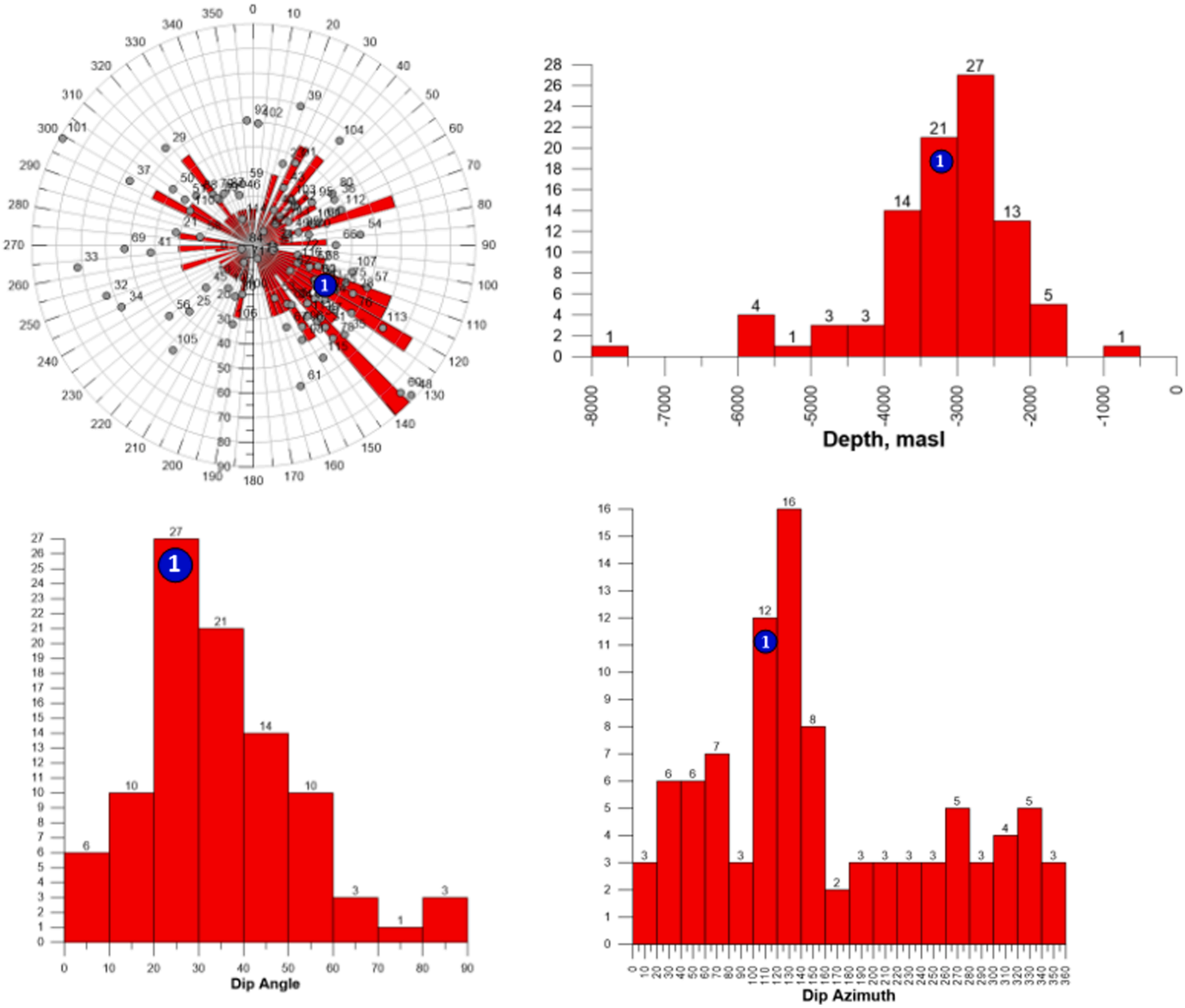

Fig. C1. This is a Fig. 3 from the main text of the paper added with seismogenic fault #1 (blue circle with a number) estimated from the most reliable sixty three MEQ's (data from "Earthquakes in Russia in the year 2009, Obninsk: GS RAN, 2009… Earthquakes in Russia in the year 2019, Obninsk: GS RAN, 2019″).
Note: Fig. 3 shows stereogram and histograms of the distribution of plane-oriented clusters of earthquakes (dip angle, dip azimuth, depth). The data were obtained from the processing of seismic data KB FIC UGS RAS of the Mutnovsky volcano (2009–2020) using the Frac-Digger program. Prevalence of dykes with a 30° dip angle and NNE strike indicate geomechanical conditions of RF horizontal compression in the NNW direction.

Then we run Frac-Digger2 with sampling criteria ($\delta_R = 6$ km, $\delta_Z = 1$ km, $N = 6$), Those criteria were the same as used for magma fracking identification in Section 2.1, except of time was not in use, since stochastic Monte-Carlo method used to find out available discreet fracture sets, which accommodate reliable hypocenters above mentioned.

Two seismogenic faults were identified:

Claster ##	Dip angle (deg)	Dip Azimuth (deg)	X m	Y m	Z m	Ks max	Number of events	Area, km^2
1	29.6	116	45,128	14,598	−3382	5.4	34	20.8
2	22.2	45	45,348	22,200	−4465	6	17	16.9

Fault #1 includes most of the hypocenters in a vicinity of Mutnovsky volcano, fault #2 includes most of the hypocenters adjacent to east of the Gorely volcano caldera rim. Both faults include 51 of 63 reliable hypocenters (81%). Geometry of the fault #1 (dip angle, dip azimuth, depth) is ideally fit to dominant geometries of magma fracking events shown in Fig. C1 (Fig. 3) and Fig. C2 (Fig. 4C). Thus, we confirmed magma fracking events described in Section 2.1 by most reliable MEQ's data set.

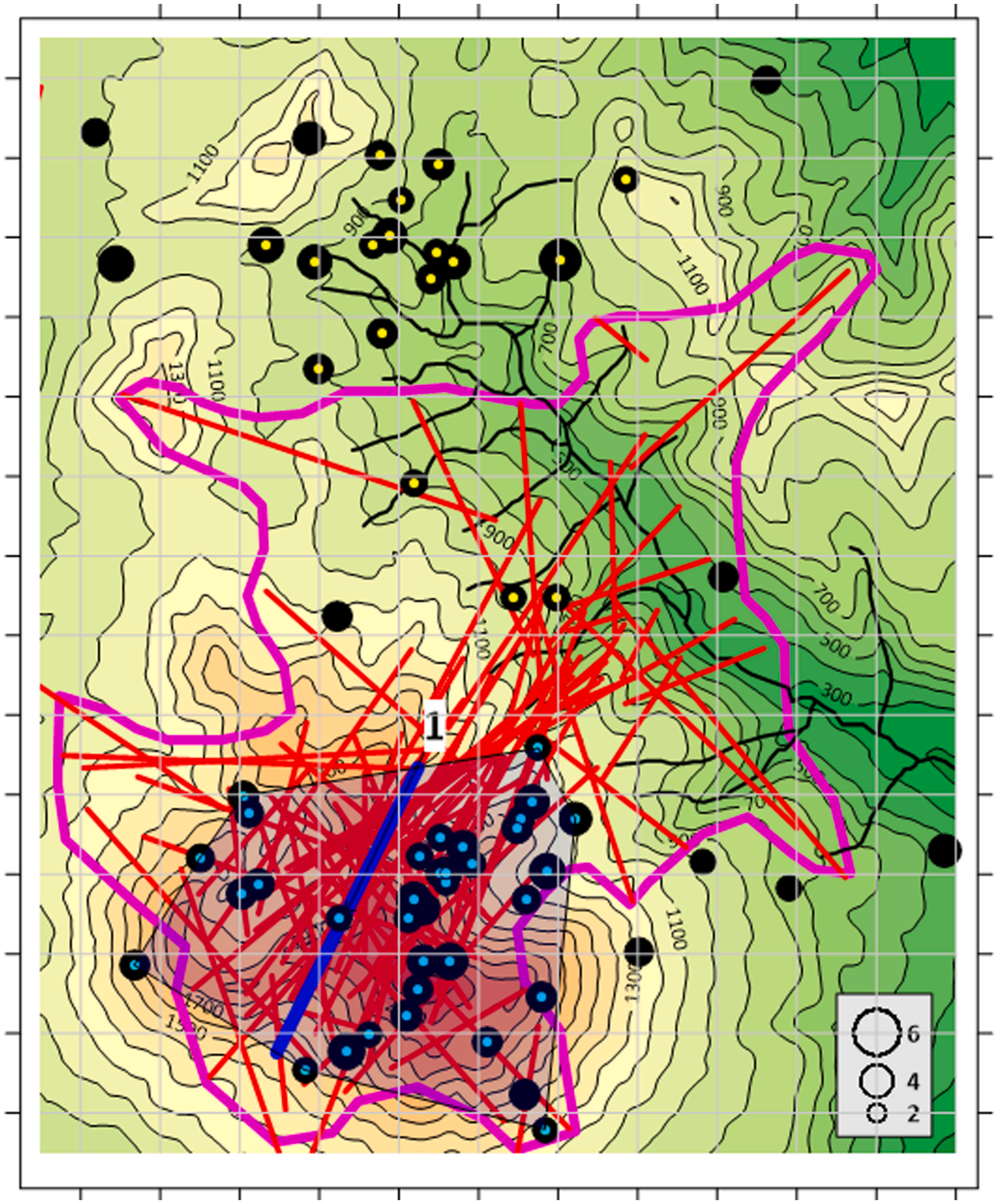

Fig. C2. This is a Figure 4C from the main text of the paper added with seismogenic fault #1 trace at −3000 m (blue thick line with a number) estimated from the most reliable sixty three MEQ's shown by circles, proportional to MEQ's magnitudes (scale is in Ks) (data from "Earthquakes in Russia in the year 2009, Obninsk: GS RAN, 2009… Earthquakes in Russia in the year 2019, Obninsk: GS RAN, 2019"). MEQ's belonging to seismogenic fault #1 are marked by light blue small circles, MEQ's belonging to seismogenic fault #2 are marked by yellow small circles, convex polygon projection of the fault #1 is highlighted by gray color.
Note: Fig. 4C shows schematic topo map of Mutnovsky geothermal area with dykes traces at elevations of −3000 m are shown by red lines, main feeding sill contours at elevation of −3000 m is shown by magenta thick line, Falshivaya river is shown by blue lines. Axes scale – 1 km, map coverage is the same as Fig. 2.

References

Asanuma, H., Mogi, T., Tsuchiya, N., Watanabe, N., Naganawa, S., Ogawa, Y., Fujimitsu, Y., Kajiwara, T., Osato, K., Shimada, K., Horimoto, S., Sato, T., Yamada, S., Watanabe, K., 2020. Japanese supercritical geothermal project for drastic increase of geothermal power generation in 2050. In: Proceedings World Geothermal Congress 2020+1.

Asaulov, G.M., et al., 1987. Report On the Results of the Exploration Works At the Dachny Site of the Mutnovsky Geothermal Field with Reserves Assessment For a 50 MWe Power Plant. Thermalny, Kamchatka.

Aiuppa, A., Giudice, G., Liuzzo, M., Tamburello, G., Allard, P., Calabrese, S., Chaplygin, I., McGonigle, A.J.S., Taran, Y., 2012. First volatile inventory for Gorely volcano, Kamchatka. Geophys. Res. Lett. 39, L06307. https://doi.org/10.1029/2012GL051177.

Chubarova, O.S., Gusev, A.A., Chebrov, V.N., 2010. The ground motion excited by the Olyutorskii earthquake of April 20, 2006 and by its aftershocks based on digital recordings. J. Volcanolog. Seismol. 4, 126–138. https://doi.org/10.1134/S0742046310020065.

Eichelberger, J., Kiryukhin, A., Mollo, S., Tsuchiya, N., Villeneuve, M., 2020a. Exploring and Modeling the Magma–Hydrothermal Regime. Geosciences (234), 10. https://doi.org/10.3390/geosciences10060234.

Eichelberger, J., Carrigan, C., Ingolfsson, H., Lavallee, Y., Ludden, J., Markusson, S., Mortensen, A., Papale, P., Sigmundsson, F., Tester, J., et al., 2020b. Magma-sourced geothermal energy and plans for Krafla magma testbed. In: Proceedings World Geothermal Congress 2020+1.

Fedotov, S.A., 1972. Energetic classification of the Kurilo-Kamchatka earthquakes and the problem of magnitudes. Ed. Moscow: Nauka (in Russian).

Fedotov, S.A., 2006. *Magmaticheskie pitayushchie systemy I mekhanizm izverzhenii vulkanov* (Plumbing systems and the mechanism of volcanic eruptions). Ed. Moscow: Nauka (in Russian).

Fedotov, S.A., Solomatin, A.V., 2019. Long-term earthquake prediction (LTEP) for the Kuril–Kamchatka island arc, June 2019 to May 2024; properties of preceding seismicity from January 2017 to May 2019. The development and practical application of the LTEP. Volcanol. Seismol. 6, 6–22. https://doi.org/10.31857/S0203-0306201966-22.

Friðleifsson, G., Pálsson, B., Albertsson, A., Stefánsson, B., Gunnlaugsson, E., Ketilsson, J., Gíslason, P., 2015. IDDP-1 drilled into magma – world's first Magma-EGS System created. In: Proceedings World Geothermal Congress 2015.

Gavrilenko, G.M., Melnikov, D.V., 2008. 15 years in life of Mutnovsky volcano. Priroda 2, 54–58 (in Russian).

Girina, O.A., Manevich, A.G., et al., 2014. Activity of volcanoes in Kamchatka in 2013. In: Proceedings of the regional conference "Volcanism and related processes" dedicated to the Day of the Volcanologist. Petropavlovsk-Kamchatsky, Russia, pp. 38–45 (in Russian).

Halldórsdóttir, S., Gudnason, E., Berre, I., Axelsson, G., Keilegavlen, E., Thorgilsson, G., 2020. Heat transfer and flow paths in the deep part of the IDDP-2 well in Reykjanes, SW Iceland. In: Proceedings World Geothermal Congress 2020+1.

Kiryukhin, A.V., 1993. High temperature fluid flows in the Mutnovsky hydrothermal system, Kamchatka. Geothermics 23 (1), 49–64. https://doi.org/10.1016/0375-6505(93)90020-N.

Kiryukhin, A.V., 1996. Modeling studies: the Dachny geothermal reservoir, Kamchatka, Russia. Geothermics 25 (1), 63–90. https://doi.org/10.1016/0375-6505(95)00035-6.

Kiryukhin, A.V., Fedotov, S.A., Kiryukhin, P.A., 2016. A geomechanical interpretation of the local seismicity related to eruptions and renewed activity on Tolbachik, Koryakskii, and Avacha Volcanoes, Kamchatka, in 2008–2012. J. Volcanolog. Seismol. 10, 275–291. https://doi.org/10.1134/S0742046316040047.

Kiryukhin, A., Norbeck, J., 2017. Analysis of magma injection beneath an active volcano using a hydromechanical numerical model. In: Proceedings 42nd Workshop on Geothermal Reservoir Engineering. Stanford University, Stanford, California, USA, pp. 740–747.

Kiryukhin, A., Lavrushin, V., Kiryukhin, P., Voronin, P., 2017. Geofluid systems of Koryaksky-Avachinsky volcanoes (Kamchatka, Russia). Geofluids 2017, 4279652. https://doi.org/10.1155/2017/4279652.

Kiryukhin, A.V., Fedotov, S.A., Kiryukhin, P.A., 2018. Magmatic systems and the conditions for hydrothermal circulation at depth in the Klyuchevskoy volcanic cluster as inferred from observations of local seismicity and thermo-hydrodynamic simulation. J. Volcanol. Seismol. 12, 231–241. https://doi.org/10.1134/S0742046318040036.

Kiryukhin, A., Polyakov, A., Kiryukhin, P., 2018. Analysis of magma injections beneath Mutnovsky volcano (Kamchatka). In: Proceedings 43-rd Workshop on Geothermal Reservoir Engineering. Stanford University, Stanford, California, USA, pp. 658–666.

Kiryukhin, A.V., Polyakov, A.Y., Usacheva, O.O., Kiryukhin, P.A., 2018. Thermal-permeability structure and recharge conditions of the Mutnovsky high temperature geothermal field (Kamchatka, Russia). J. Volcanol. Geotherm. Res. 356, 36–55. https://doi.org/10.1016/j.jvolgeores.2018.02.010.

Kiryukhin A. V. Modeling of the Dachny Site Mutnovsky Geothermal Field (Kamchatka, Russia) in Connection with the Problem of Steam Supply for 50 MWe Power Plant. Proc.World Geothermal Congress 2005 Antalya, Turkey, 2429 April 2005. 12 p.

Kiryukhin, A.V., 2020. Geothermofluidomechanics of hydrothermal, volcanic and hydrocarbon systems. Ed.: St. Petersburg, Eko-Vector I-P (in Russian). https://www.elibrary.ru/item.asp?id=45739830.

Kiryukhin, A.V., Sugrobov, V.M., 2019. The geothermal resources of kamchatka and the immediate prospects of their extraction. J. Volcanol. Seismology 13 (6), 389–402.

Kiryukhin, P.A., Kiryukhin, A.V., 2016. Frac-Digger. Certificate of state registration of computer programs # 2016612168 of 21.06.2016.

Kiryukhin, P.A., Kiryukhin, A.V., 2017. Frac-Digger2. Certificate of State Registration of Computer Programs # 2017618050 of 21.09.2017.

Kiryukhin, A.V., Polyakov, A.Y., Zhuravlev, N.B., Tsuchiya, N., Rychkova, T.V., Usacheva, O.O., Dubrovskaya, I.K., 2022. Dynamics of natural discharge of the hydrothermal system and geyser eruption regime in the Valley of Geysers, Kamchatka. Appl. Geochem. 136, 105166 https://doi.org/10.1016/j.apgeochem.2021.105166.

Kiryukhin, A.V., Takahashi, M., Poliakov, A.Yu., 1999. Origin of Water in the Mutnovsky Geothermal Field An Oxygen (δ18O) and Hydrogen (δD) Study Study. J. Volcanol. Seismology J. Gordon & Breach Science Publish. 20, 441–450.

Lavallée, Y., Lamur, A., Kendrick, J., Eggertsson, G., Weaver, J., Eichelberger, J., Papale, P., Sigmundsson, F., Dingwell, D., Markússon, S., Mortensen, A., Friðleifsson, G., Carrigan, C., Ludden, J., Ingólfsson, H., KMT-consortium, the, 2020. Thermal manipulation of magma boundaries: advancing controls on fluid flow via the Krafla Magma Testbed (KMT). In: Proceedings World Geothermal Congress 2020 +1.

Lolli, B., Gasperini, P., Vannucci, G., 2014. Empirical conversion between teleseismic magnitudes (m_b and M_s) and moment magnitude (M_W) at the Global, Euro-Mediterranean and Italian scale. Geophys. J. Int. 199 (2), 805–828. https://doi.org/10.1093/gji/ggu264.

McClure, M.W., 2012. Modeling and Characterization of Hydraulic Stimulation and Induced Seismicity in Geothermal and Shale Gas Reservoirs. Stanford University, Stanford, California, USA. PhD Thesis.

McClure, M., 2014. CFRAC (version 1.2) Complex Fracturing Research Code Users Guide (version 20), p. 88.

McClure, M.W., Horne, R.N., 2013. Discrete Fracture Network Modeling of Hydraulic Stimulation: Coupling Flow and Geomechanics. Springer. https://doi.org/10.1007/978-3-319-00383-2.

Muraoka, H., Uchida, T., Sasada, M., Yagi, M., Akaku, K., Sasaki, M., Yasukawa, K., Miyazaki, S., Doi, N., Saito, S., Sato, K., Tanaka, S., 1998. Deep geothermal resources survey program: igneous, metamorphic and hydrothermal processes in a well encountering 500 °C at 3729m depth, Kakkonda, Japan. Geothermics 27, 507–534. https://doi.org/10.1016/S0375-6505(98)00031-5.

Selyangin, O.B., 1993. Mutnovsky volcano, Kamchatka: new evidence on structure, evolution and future activity. J. Volcanol. Seismol. 15, 17–38.

Selyangin, O.B., 2009. Wonderful World of Mutnovsky and Gorely Volcanoes: Volcanologic and Traveller's Guide. Novaja kniga, Petropavlovsk-Kamchatsky.

Sigurdsson, O., 2020. Stimulation of the RN-15/IDDP-2 well at Reykjanes attempting to create an EGS System. In: Proceedings World Geothermal Congress 2020+1.

Simon, A., Yogodzinski, G.M., Robertson, K., Smith, E., Selyangin, O., Kiryukhin, A., Mulcahy, S.R., Walker, J.D., 2014. Evolution and genesis of volcanic rocks from Mutnovsky volcano, Kamchatka. J. Volcanol. Geotherm. Res. 286, 116–137. https://doi.org/10.1016/j.jvolgeores.2014.09.003.

Spektor, S.V., Platonova, A.V., et al., 2016. Report On "Additional Geological Study and Reserves Estimation of the Mutnovsky Geothermal Field (Update on 31.12.2015). Petropavlovsk-Kamchatsky.

Tsuchiya, N., 2020. Geological Model and Potential of Supercritical Geothermal Reservoir. In: Proceedings World Geothermal Congress 2020+1.

Usacheva, O.O., Rychkova, T.V., 2020. Analysis of the effectiveness of directional drilling in the Mutnovsky geothermal field. In: Proceedings of the Annual XXIII Scientific Conference dedicated to the Day of the Volcanologist. Petropavlovsk-Kamchatsky, Russia, pp. 223–226 (in Russian).

Vakin, E.A., Pilipenko, G.F., Sugrobov, V.M., 1986. General features of the Mutnovsky geothermal field and prognostic estimate of the resources. In: Sugrobov, V.M. (Ed.), Geochemical and Geothermal Methods of High-Temperature Thermal Field Investigation. Nauka, Moscow, pp. 6–41 (in Russian).

Zemletryaseniya Rossii v 2009g, 2019. (Earthquakes in Russia in the Year 2009), Obninsk: GS RAN, 2009 Zemletryaseniya Rossii v 2019g. (Earthquakes in Russia in the Year 2019). GS RAN, Obninsk.

Zoback, M.D., 2010. Reservoir Geomechanics. Cambridge University Press. https://doi.org/10.1017/CBO9780511586477.